The Thesis Committee for Jacqueline Patrice Maleski
Certifies that this is the approved version of the following thesis:

Direct shear wave polarization corrections at multiple offsets for anisotropy analysis in multiple layers

APPROVED BY
SUPERVISING COMMITTEE:

Supervisor:

Robert Tatham

Kyle Spikes

Paul Krail

Direct shear wave polarization corrections at multiple offsets for anisotropy analysis in multiple layers

by

Jacqueline Patrice Maleski, B.S.

Thesis

Presented to the Faculty of the Graduate School of

The University of Texas at Austin

in Partial Fulfillment

of the Requirements

for the Degree of

Master of Science in Geological Sciences

The University of Texas at Austin

May 2014

Dedication

Dedicated to my father, Jim.

Acknowledgements

I would like to thank Dr. Robert Tatham for his supervision in the completion of this work and his guidance throughout my graduate degree. I would also like to thank the members of my committee, Kyle Spikes and Paul Krail. I am particularly grateful for the knowledge and perseverance that Kyle has shared with me, which have been invaluable in completing my graduate degree. Margo Grace, Tom Hess, and Philip Guerrero have provided crucial help with the many problems I have encountered while at the University of Texas at Austin. I have the deepest gratitude for my fellow students, many of whom have become cherished friends. Sarah Coyle, Lauren Becker, Han Liu, Qi Ren, Russell Carter, Meijuan Jiang, Makoto Sadahiro, and Elliot Dahl have made the office an all too enjoyable workplace with their endearing companionship and inspiring work ethic. Lastly, I would like to give special thanks to my mother, Pam, sister, Cassie, and the rest of my family and friends for their love and support.

Abstract

Direct shear wave polarization corrections at multiple offsets for anisotropy analysis in multiple layers

Jacqueline Patrice Maleski, M.S. Geo. Sci

The University of Texas at Austin, 2014

Supervisor: Robert Tatham

Azimuthal anisotropy, assumed to be associated with vertical, aligned cracks, fractures, and subsurface stress regimes, causes vertically propagating shear waves to split into a fast component, with particle motion polarized parallel to fracture strike, and a slow component, with particle motion polarized perpendicular to fracture strike. Determining the polarization of each split shear wave and the time lag between them provides valuable insight regarding fracture azimuth and intensity. However, analysis of shear wave polarizations in seismic data is hampered by reflection-induced polarization distortion. Traditional polarization analysis methods are limited to zero offset and are not valid if implemented over the full range of offsets available in typical 3D seismic data sets. Recent proposals for normalizing amplitudes recorded at non-normal incidence to values recorded at normal incidence may provide an extension to correcting offset-dependent shear wave polarization distortion. Removing polarization distortion from shear wave reflections allows a larger range of offsets to be used when determining shear wave polarizations. Additional complexities arise, however, if fracture orientation

changes with depth. Reflections from layers with different fracture orientations retain significant energy on off-diagonal components after initial rotations are applied. To properly analyze depth-variant azimuthal anisotropy, time lags associated with each interval of constant anisotropy are removed and additional iterative rotations applied to subsequent offset-normalized reflections. Synthetic data is used to evaluate the success of these methods, which depends largely on the accuracy of AVA approximations used in the correction. The polarization correction effectively removes SV polarity reversals but may be limited in corrections to SH polarizations at very far offsets. After the polarization correction is applied, energy calculations including incidence angles up to 20° more effectively compensates individual SV and SH reflection components, allowing for more faithful polarization information identification of the isotropy plane and the symmetry axis. The polarization correction also localizes diagonal component energy maxima and off-diagonal component energy minima closer to the true orientation of the principal axes when a range of incidence angles up to 20° is used.

Table of Contents

List of Tables

List of Figures

Chapter 1: Introduction

1.1 AZIMUTHAL ANISOTROPY

Vertical, aligned cracks, fractures, and subsurface stress regimes are predominant causes of azimuthal anisotropy (Figure 1.1). Many low porosity, low permeability carbonate and shale reservoirs contain natural fractures, which impact fluid flow during production (Aguilera, 1980; Nelson, 1985). In shales and tight sandstones that also have low matrix porosity and permeability, anisotropy due to parallel bedding is less significant compared to fracture-related anisotropy for near-vertical shear-wave propagations (Li, 1997). Proper characterization of fracture geometry and distribution is key to the successful development of both conventional and unconventional naturally fractured reservoirs. Failure to account for the presence and effect of natural fractures can lead to irreparable loss of recovery, primary recovery patterns that are inappropriate for secondary recovery, inefficient capital expenditure during development, drilling of unnecessary in-fill wells, and improper assessment of economic opportunities (Nelson, 1985). Determining preferred subsurface stress directions can also help to minimize borehole stability problems in well drilling plans (Thomsen et al., 1999). Assessing the effects of natural fractures and subsurface stress conditions in reservoirs is of primary importance so that proper planning and evaluation can be implemented from the beginning.

Figure 1.1: Vertical, aligned cracks, fractures, and subsurface stress regimes are common causes of azimuthal anisotropy.

Crack and fracture orientation and magnitude might vary with depth if remnants of a paleostress regime have been preserved, despite conditions of the current stress regime, through cementation or crystallization processes (Lynn and Thomsen, 1986). Additionally, the orientation and magnitude of the maximum horizontal stress might vary with depth in the proximity of major stratigraphic discontinuities or faulting (Winterstein and Meadows, 1991a, b). Hickman et al. (1988) suggest that combinations of fault-normal compression and traditional strike-slip stress configuration may vary locally,

leading to changes in stress magnitude and orientation that modify the geometry of fluid-filled microcracks and fractures. Haacke et al. (2009) attribute vertical changes in the direction of maximum horizontal stress to a transition from a gravitational, slope-related stress regime in shallow sediments to transform-related stress regime in deeper sediments. Warpinski and Teuful (1991) observed up to 45° degree changes in stress orientation between interlayered tuffs of varying mechanical strength. Their results show that stress magnitudes in adjacent layers can be relatively independent of each other, whereby stiff layers of hard, brittle rock support regional stresses, and softer beds decouple into separate, disjointed stress fields. Beckham (1996) observe three changes in azimuthal anisotropy orientation across fractured carbonates in Oklahoma.

1.2 SHEAR-WAVE SPLITTING

A shear wave propagating vertically through azimuthally anisotropic media will split into two orthogonally polarized components (Figure 1.2). Particle motion of the fast shear wave (S1) is oriented parallel to the maximum horizontal stress or fracture strike, i.e., in the stiffest direction. Particle motion of the slow shear wave (S2) is oriented parallel to the most compliant direction, and perpendicular to S1. The time delay between each component is related to the length of the raypath within the anisotropic medium as well as the magnitude of anisotropy along that specific raypath. Anisotropy caused by vertical, aligned fractures, microfractures, or isolated microcracks decreases the velocity of the slow shear wave but not the fast shear wave. The reduced slow shear wave velocity causes a relative change in impedance contrast for fast and slow modes, and differential normal-incidence reflectivity of fast and slow shear modes can thus provide a qualitative estimate of lateral fracture variability.

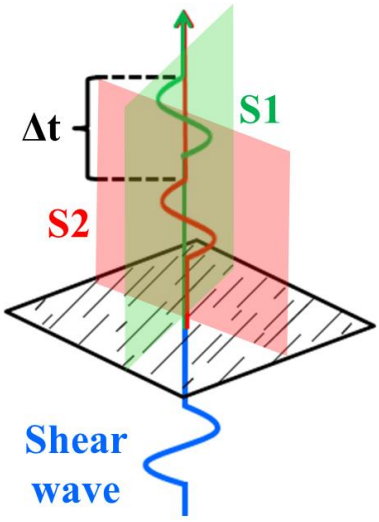

Figure 1.2: A shear wave propagating vertically through azimuthally anisotropic media splits into two components with orthogonal polarizations. Particle motion of the fast shear wave (S1) is oriented parallel to the maximum horizontal stress or fracture strike, i.e., in the stiff direction. Particle motion of the slow shear wave (S2) is oriented parallel to the compliant direction, and perpendicular to S1. Adapted from Tatham and McCormack (1991).

In the presence of depth-variant azimuthal anisotropy, each pure shear mode will progressively split into two modes aligned according to the anisotropy system in each new layer it encounters on both down-going and up-going raypaths (Figure 1.3). The fast and slow modes in each pair of arrivals polarize according to the most recent anisotropy system encountered along the raypath. In reflection surveys, this corresponds to the shallowest layer. Information about anisotropy within deeper layers is obscured by the anisotropic overburden. Moreover, if the path length is short or the magnitude of anisotropy is small, split shear wave arrivals will interfere deconstructively, obscuring interpretations about polarization, delay time, and the normal incidence reflection coefficient.

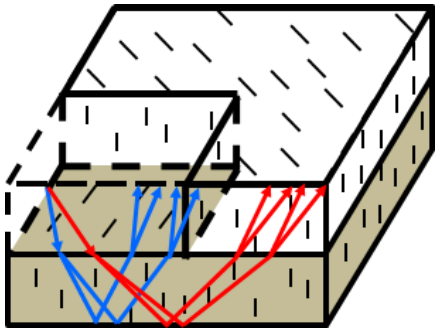

Figure 1.3: A medium in which the principal axes of anisotropy change within finite intervals at different depths causes each pure shear mode to split progressively into two modes aligned according to the anisotropy system in each new layer they encounter on both down-going and up-going paths. Adapted from Thomsen et al. (1999).

Shear-wave splitting has been confirmed in many sedimentary basins of interest to hydrocarbon exploration. This splitting has been confirmed from converted P-to-S waves in surface-to-surface measurements (Harrison and Stewart, 1993), converted P-to-S waves in surface-to-borehole measurements (Garotta and Granger, 1988; Lefeuvre and Queen, 1992), pure S-waves in surface-to-surface measurements (Alford, 1986; Davis and Lewis, 1990; Lynn and Thomsen, 1990; Mueller, 1991) and pure S-waves in surface-to-borehole measurements (Cliet et al., 1991; MacBeth and Crampin, 1991; Winterstein and Meadows, 1991a, b; Lefeuvre et al., 1992, 1993; Queen et al., 1992). Therefore, it is important to evaluate what information can be extracted reliably from shear-wave data and to establish consistent processing sequences to extract such information. In this study, I will deal solely with direct shear-wave sources.

Liu and Crampin (1990), Liu et al. (1990), Yardley and Crampin (1991) and Yardley et al. (1991) investigated the variability of shear-wave polarizations and amplitudes in synthetic multicomponent VSPs and reflection profiles. Alford (1986), Thomsen (1988), Li and Crampin (1993), and Winterstein and Meadows (1991a, b) developed techniques for extracting shear-wave attributes such as polarization, time

delay, and amplitude variation in VSPs and 3D multicomponent reflection data. The results of these studies, among many others, have shown that information contained in shear-waves, such as polarization, delay time, and normal incidence reflection coefficients enables more effective characterization of natural anisotropy systems than P-waves alone. By using direct shear-sources for characterization of anisotropy with polarization consideration, we can limit any negative effects of inhomogeneity by employing a single ray-propagation path for the analysis. However, the abovementioned studies have also drawn attention to the many complexities inherent to the transmission and reflection of transversely polarized waves at internal interfaces and the free surface. The proposed polarization corrections allow for a reduction in these complexities at reflective interfaces.

1.3 SHEAR WAVE POLARIZATION DISTORTION

Booth and Crampin (1985) identified a "shear wave window" of about 30°, outside of which a recorded shear wave incident upon a free surface exhibits significant phase and polarization distortion, even in isotropic media. Liu and Crampin (1990) adopted the shear wave window concept to assess the effects of polarization distortion upon transmission across an internal interface and again found that shear wave polarizations become increasingly distorted at larger angles of incidence. In further studies, Liu et al. (1990) observed the 180° phase reversal from emitted source polarizations of reflected shear waves at incidence angles near 20° for an isotropic-isotropic interface. The authors concluded that such large variations in shear-wave polarizations weaken shear-wave reflections in stacked common depth point (CDP) gathers. Moreover, if the shear wave source polarization is not parallel to receiver orientation, shear wave reflections will be recorded as a vectorial combination of their

true source polarizations. Further, even if the shear source polarization and receiver orientation are aligned, but the source-receiver azimuthal direction is not aligned, polarization will not be properly represented. Field data must be transformed into proper radial and transverse coordinates according to the angle between each source-receiver pair in order to analyze individual vertically or horizontally polarized shear waves. Until data are represented in radial and transverse components, and the differences in reflectivity for the SV- and SH- components reconciled, the presence of anisotropy cannot be properly validated.

In the case of an isotropic-anisotropic interface, if the principal axes of the underlying anisotropy system are not aligned parallel to the incident shear wave polarizations, the wave will polarize into alignment with the underlying anisotropy system upon reflection (Campbell and Tatham, 2013). This change in polarization is much like shear-wave splitting upon transmission through anisotropic media, though no time lag accumulates. The change in polarization results from a difference in reflection coefficients for a wave parallel and perpendicular to the isotropy plane of the lower layer's anisotropy system (i.e., crack strike, maximum horizontal stress). Thus, when azimuthal anisotropy is present, the preference is to transform field data into alignment with the coordinates of the natural anisotropy system. These coordinates correspond to the fast and slow components of each split shear wave. After identifying individual fast and slow shear wave components, quantitative analysis of shear wave attributes such as polarization, time delay, and differential normal incidence reflectivity can be performed to assess anisotropy characteristics such as maximum horizontal stress or fracture strike, fracture intensity, and lateral variability.

1.4 CORRECTING SHEAR WAVE POLARIZATIONS

Much of the analysis of direct shear-shear reflections has been limited to near-offsets and near-normal incidence angles. Shear wave polarization and phase distortion reported by Booth and Crampin (1985), Liu and Crampin (1990), and Liu et al. (1990) hampers use of an increasing range of offsets and larger incidence angles beyond critical angles available in many modern 3D seismic surveys.

Lyons (2006) proposed a method to correct shear-wave polarization distortion in isotropic media, allowing extension (Campbell and Tatham, 2013) of traditional rotation algorithms (Alford, 1986) to non-normal angles of incidence. Campbell and Tatham (2012, 2013) further extended the concept to include the case of a single isotropic-anisotropic interface. The efficacy of these methods has yet to be assessed in the presence of depth-variant azimuthal anisotropy, where anisotropic-anisotropic interfaces occur in a series of layers. To analyze changes in shear-wave polarization with depth, a layer-stripping (Winterstein and Meadow, 1991a, b) approach must be implemented in conjunction with traditional rotation algorithms. I present synthetic data to evaluate the effectiveness of previously proposed shear-wave polarization corrections in the presence of depth-variant azimuthal anisotropy using non-normal incidence angles.

Chapter 2: Background Information

2.1 SHEAR WAVES IN ISOTROPIC MEDIA

2.1.1 Reflectivity

Zoeppritz (1919) derived mathematical expressions for elastic plane wave reflectivity at a welded interface between two half-spaces with differing elastic properties in the late nineteenth and early twentieth centuries. Aki and Richards (2002) provide a comprehensive representation of the P-, SV-, and SH-wave reflection coefficients as a function of incidence angle originally derived by Knott and Zoeppritz. Particle motions for P- and SV-waves are contained within the same plane, and their reflection strengths are, therefore, mechanically coupled in the reflection-refraction-mode conversion process.

Figure 2.1 summarizes 16 possible waves that can result from a P- or SV- wave incident upon a welded interface between two solid half-spaces with different elastic properties. Down-ticks denote downward travelling waves, and up-ticks denote upward travelling waves. The reflection, transmission, and conversion coefficients of an incident P- or SV- wave can be organized into a 4x4 scattering matrix,

$$\begin{pmatrix} \grave{P}\acute{P} & \grave{S}\acute{P} & \acute{P}\acute{P} & \acute{S}\acute{P} \\ \grave{P}\acute{S} & \grave{S}\acute{S} & \acute{P}\acute{S} & \acute{S}\acute{S} \\ \grave{P}\grave{P} & \grave{S}\grave{P} & \acute{P}\grave{P} & \acute{S}\grave{P} \\ \grave{P}\grave{S} & \grave{S}\grave{S} & \acute{P}\grave{S} & \acute{S}\grave{S} \end{pmatrix} = M^{-1}N. \qquad 2.1$$

The first column in Equation 2.1 defines reflected, mode converted, and refracted waves resulting from a downward travelling P-wave incident on the interface depicted in Figure 2.1a. The second column in Equation 2.1 defines reflected, mode converted, and

refracted waves resulting from a downward travelling SV-wave incident on the interface depicted in Figure 2.1b. The third column in Equation 2.1 defines reflected, mode converted, and refracted waves resulting from a upward travelling P-wave incident on the interface depicted in Figure 2.1c. The fourth column in Equation 2.1 defines reflected, mode converted, and refracted waves resulting from a upward travelling SV-wave incident on the interface depicted in Figure 2.1d.

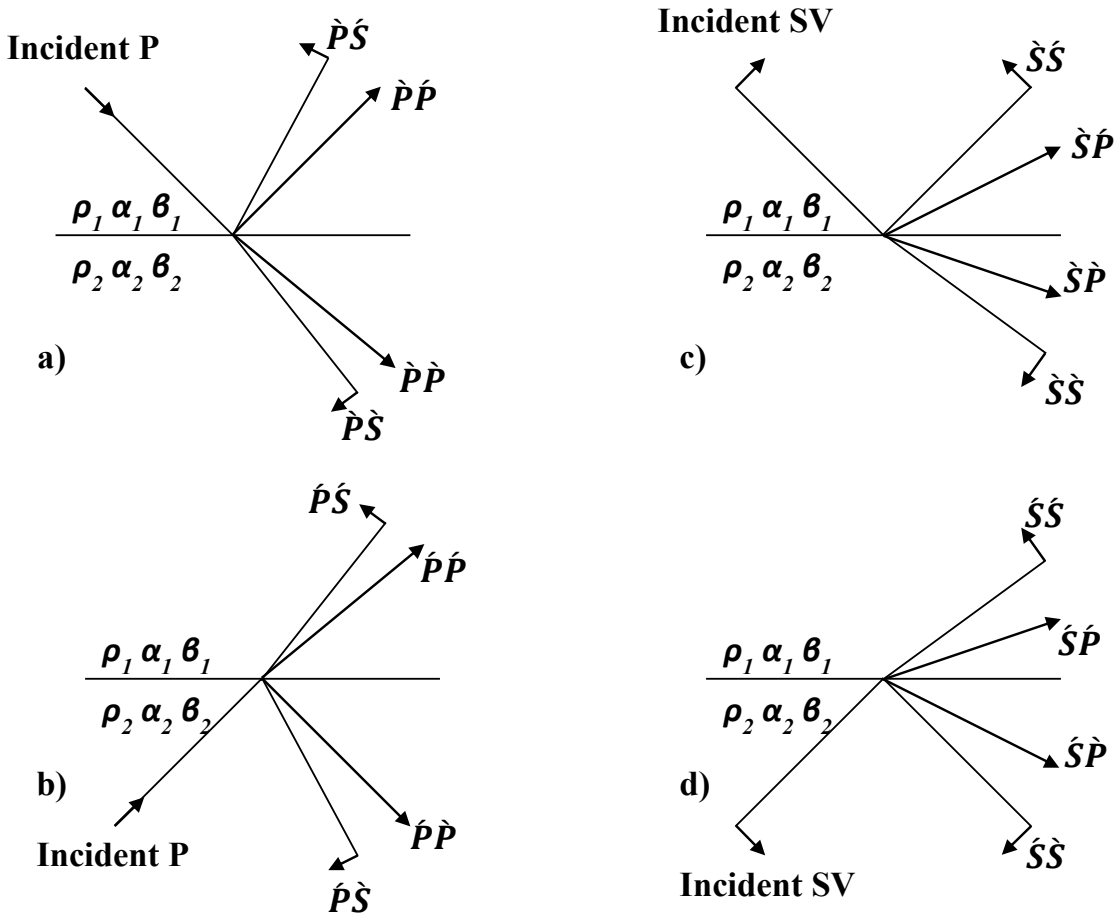

Figure 2.1: Reflected, transmitted, and converted waves for incident P- and SV-waves at an interface between two solid half-spaces with different elastic properties. Short arrows show the direction of particle motion. Adapted from Aki and Richards (2002).

This system of equations can be further expressed as a combination of elastic properties and incidence angles to solve for reflection, transmission, and conversion coefficients of all possible scattered waves shown in Figure 2.1. The matrices M and N given in equation 2.1 may be represented in terms of the velocities α_1, α_2, β_1, β_2, and the ray parameter, p,

$$p = \frac{\sin i_1}{\alpha_1} = \frac{\sin j_1}{\beta_1} = \frac{\sin i_2}{\alpha_2} = \frac{\sin j_2}{\beta_2}, \qquad 2.2$$

$$M = \begin{pmatrix} -\alpha_1 p & -\cos j_1 & \alpha_2 p & \cos j_2 \\ \cos i_1 & -\beta_1 p & \cos i_2 & -\beta_2 p \\ 2\rho_1\beta_1^2 p\cos i_1 & \rho_1\,\beta_1(1-2\beta_1^2 p^2) & 2\,\rho_2\,\beta_2^2\,p\cos i_2 & \rho_2\beta_2(1-2\beta_2^2 p^2) \\ -\rho_1\alpha_1(1-2\beta_1^2 p^2) & 2\rho_1\beta_1^2 p\cos j_1 & \rho_2\alpha_2(1-2\beta_2^2 p^2) & -2\rho_2\beta_2^2 p\cos j_2 \end{pmatrix} \qquad 2.3$$

$$N = \begin{pmatrix} \alpha_1 p & \cos j_1 & -\alpha_2 p & -\cos j_2 \\ \cos i_1 & -\beta_1 p & \cos i_2 & -\beta_2 p \\ 2\rho_1\beta_1^2 p\cos i_1 & \rho_1\,\beta_1(1-2\beta_1^2 p^2) & 2\,\rho_2\,\beta_2^2\,p\cos i_2 & \rho_2\beta_2(1-2\beta_2^2 p^2) \\ \rho_1\alpha_1(1-2\beta_1^2 p^2) & -2\rho_1\beta_1^2 p\cos j_1 & -\rho_2\alpha_2(1-2\beta_2^2 p^2) & 2\rho_2\beta_2^2 p\cos j_2 \end{pmatrix} \qquad 2.4$$

In two-dimensions, SH-waves are not mechanically coupled to either P- or SV-waves, so SH-wave reflectivity behavior is, therefore, significantly simplified. Reflection

and transmission coefficients for SH-waves can now be organized into a 2x2 scattering matrix:

$$\begin{pmatrix} \grave{S}\acute{S} & \acute{S}\acute{S} \\ \grave{S}\grave{S} & \acute{S}\grave{S} \end{pmatrix} \quad 2.5$$

where column one defines reflected (row one) and transmitted (row two) waves resulting from a downward travelling SH-wave incident upon the interface. Column two defines transmitted (row one) and reflected (row two) waves resulting from an upward travelling SH-wave incident upon the interface. The reflected SH-wave can be represented as a combination of elastic properties and incidence angles

$$\grave{S}\acute{S} = \frac{\rho_1\beta_1 cosj_1 - \rho_2\beta_2 cosj_2}{\rho_1\beta_1 cosj_1 + \rho_2\beta_2 cosj_2} \quad 2.6$$

where the elements are the same as in equation 2.1, 2.2, and 2.3.

Reflection coefficients as a function of incidence angle in degrees are shown in Figure 2.2 for vertically (SV) and horizontally (SH) polarized pure shear waves reflected from an interface with properties defined in Table 2.1. SH-SH reflection coefficient values do not vary significantly from normal-incidence values across a large range of incidence angles, up to about 20°. Beyond 20° incidence angle, reflection coefficient values begin to increase, approaching a polarity reversal at about 40°. At this angle, only energy polarized normal to the incident plane (i.e., SV energy) is reflected, and SH reflections are not observed. Beyond 40° incidence angle, SH-SH reflection coefficient values increase rapidly.

	V_P (km/s)	V_S (km/s)	Density (g/cm^3)
Layer 1	4	2	2.2
Layer 2	5	2.5	2.4

Table 2.1: Isotropic model parameters used for approximations to Zoeppritz equations.

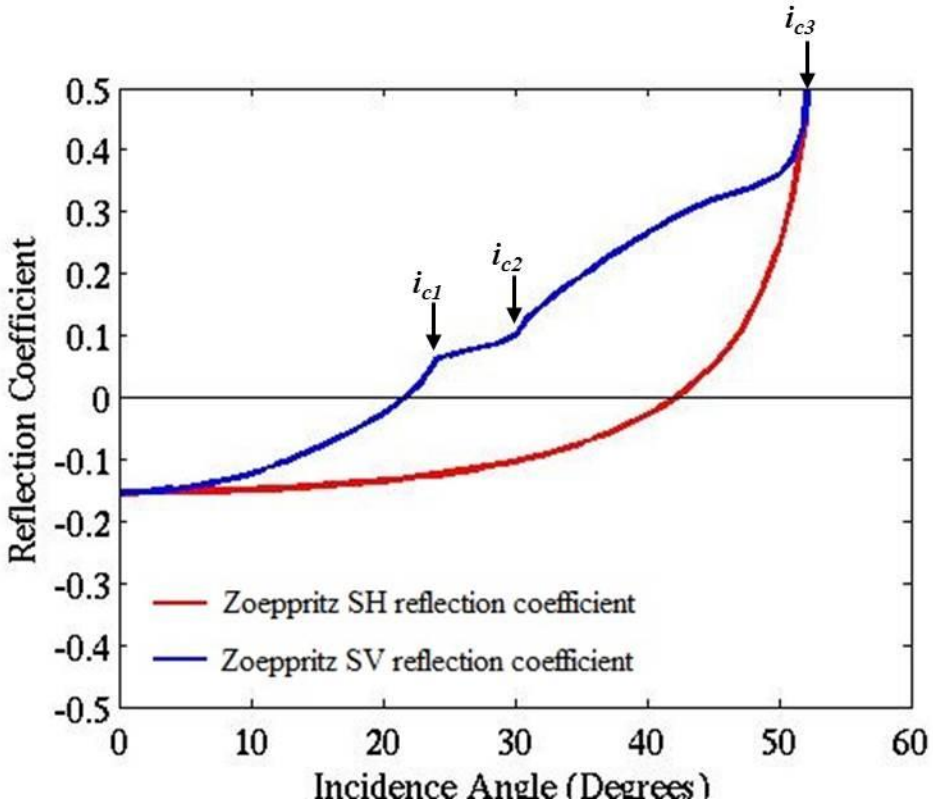

Figure 2.2: Zoeppritz reflection coefficients as a function of incidence angle in degrees for vertically (SV) and horizontally (SH) polarized pure shear waves. SH-SH reflectivity remains consistent with normal incidence values across a large range of incidence angles, up to about 20°, where reflection coefficient values begin increasing and eventually undergo a polarity reversal at about 40°. However, SV-SV reflectivity diverges from normal incidence values at relatively modest incidence angles. SV reflection coefficient values increase rapidly as the curve approaches a polarity reversal at approximately 20°. Due to complex coupled interactions between SV and P modes, the SV-SV reflectivity exhibits unstable behavior across not only the polarity reversal at about 20°, but near three critical angles, at 24°, 30°, and 53°as well. Beyond the critical angle at 53°, both SV and SH reflection coefficients increase rapidly as each wave undergoes total internal reflection.

SV-SV reflectivity behaves more erratically than SH-SH reflectivity, diverging from normal incidence values at a much faster rate. This behavior is related to complex coupled interactions between SV and P modes, which cause three critical angles to occur for a single SV wave incident upon an interface with increasing impedance. The first critical angle occurs as the incident SV wave is converted to a P wave upon transmission through the interface. This critical angle can be observed at a relatively modest incidence angles, approximately 24° ($\sin^{-1}(V_{S1}/V_{P2})$), and corresponds to the limit of transmitted mode-converted P waves. For incidence angles beyond the smallest critical angle, coefficients of the previously real transmitted wave become complex. An additional critical angle occurs as the incident SV wave is converted to an internal P wave reflection at the interface, observed at 30° ($\sin^{-1}(V_{S1}/V_{P1})$) in Figure 2.2. This angle corresponds to the limit of reflected, mode-converted P waves. The last critical angle occurs at approximately 53° ($\sin^{-1}(V_{S1}/V_{S2})$) incidence angle and marks the limit of transmitted shear waves. Beyond this critical angle, all incident shear waves undergo total internal reflection.

Shear wave critical angles also correspond to points where the incident wavelet phase shows abrupt and significant deviations in phase. Again, SV waves show considerably greater variation in phase at much smaller angles of incidence relative to SH waves (Figure 2.3). At the first critical angle, i_{c1}, at 24°, the SV wave begins approaching minimum phase until reaching the second critical angle, i_{c2}, at 30°. At this point, a local maximum is observed, but SV phase remains negative. SV phase then decreases phase until reaching the third critical angle, i_{c3}, at 53°. At this critical angle, which marks the onset of total internal reflection, both SV and SH phase show wide variation from zero phase.

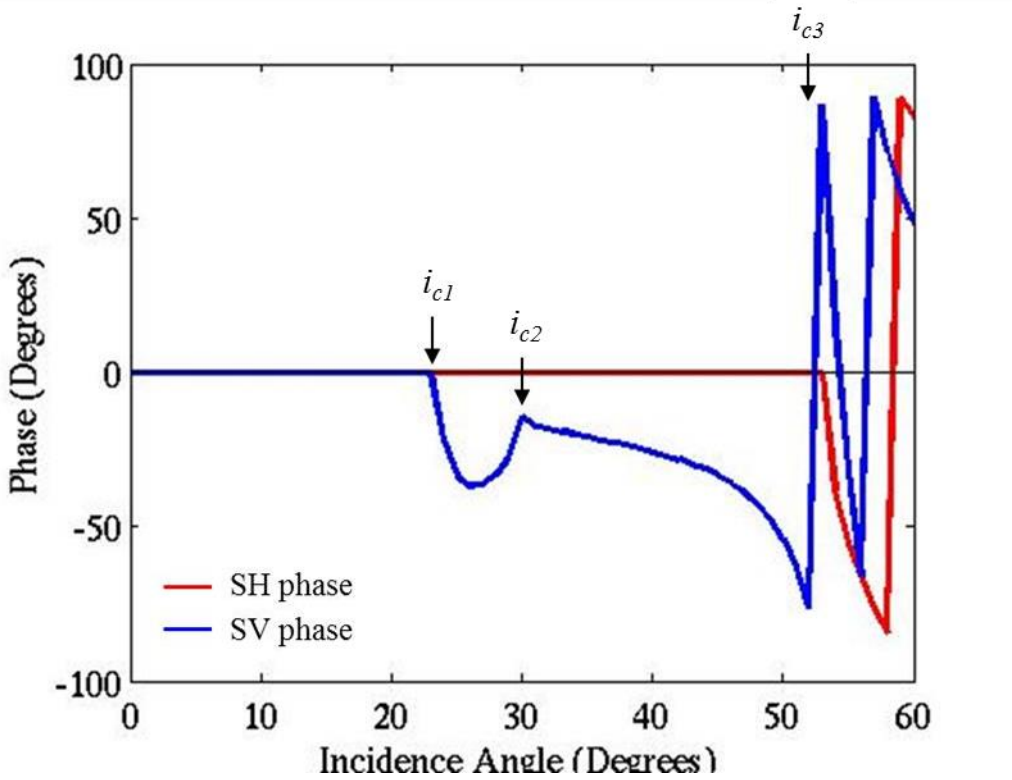

Figure 2.3: Phase of SH (red) and SV (blue) reflected energy in degrees as a function of incidence angle in degrees. Beyond the first SV critical angle, i_{c1}, at 24°, the phase of the incident wave begins to deviate from zero-phase up to a maximum phase of about 35°. Near the third critical angle, i_{c3}, which marks the onset of total internal reflection, both SV and SH phase vary significantly from zero-phase.

The important features of shear wave reflectivity in regards to this work are their reflection amplitudes at normal incidence. As the angle of incidence increases, the reflectivity curves diverge from their normal incidence values. Given that the reflectivity behavior of SV and SH waves is quite different over a wide range of incidence, the results of CDP stacking also differ for each wave mode. SV amplitudes and polarizations observed beyond 20° incidence angle will be of comparable strength to amplitudes and polarizations observed below 20° incidence angle, but possess the opposite polarity. The SV wave polarity reversal that occurs near 20° incidence angle may thus have

deconstructive consequences, weakening or possibly canceling post-stack SV reflection events. In contrast, SH waves behave more consistently over a larger range of incidence angles, and stacking would not have such deleterious effects.

2.1.2 Shear wave AVO approximations

The complexity of the full Zoeppritz equations has given rise to numerous simplifying approximations. Spratt et al. (1993) developed one such approximation for SV-wave AVO under the assumption of small velocity and density contrasts across an interface:

$$\grave{S}\acute{S}_{SV} = -\frac{1}{2}(1 - 4\beta^2 p^2)\frac{\Delta\rho}{\bar{\rho}} - \left(\frac{1}{2cos^2\theta} - 4\beta^2 p^2\right)\frac{\Delta\beta}{\bar{\beta}} \qquad 2.7$$

where $\grave{S}\acute{S}_{SV}$ SV reflectivity, $\bar{\beta}$ is the average shear wave velocity, p is the ray parameter, $\bar{\rho}$ the average density, θ is the incident angle, $\Delta\beta$ is the shear velocity contrast, and $\Delta\rho$ is the density contrast. For small incident angles (less than 30°) and a V_P/V_S ratio equal to 2, the above approximation simplifies to

$$\grave{S}\acute{S}_{SV} = -R_S + \left[7R_{SV} + \frac{1}{2}\left(\frac{\Delta\rho}{\bar{\rho}}\right)\right] sin^2\theta \qquad 2.8$$

where

$$R_S = \frac{1}{2}\left(\frac{\Delta\rho}{\bar{\rho}} + \frac{\Delta\beta}{\bar{\beta}}\right). \qquad 2.9$$

Using this approximation, SV-wave reflectivity can be expressed with two terms whose individual contributions to near- and far-offset components are easily identified:

$$\grave{S}\acute{S}_{SV} = A + Bsin^2\theta \tag{2.10}$$

where

$$A = -\frac{1}{2}\left(\frac{\Delta\rho}{\bar{\rho}} + \frac{\Delta\beta}{\bar{\beta}}\right) \tag{2.11}$$

controls near-offset reflectivity and

$$B = 7R_S + \frac{1}{2}\left(\frac{\Delta\rho}{\bar{\rho}}\right) \tag{2.12}$$

controls far-offset reflectivity. Figure 2.4 shows Zoeppritz (solid) and Spratt (dashed) reflection coefficients for an SV wave incident on an interface with medium properties described in Table 2.1. The zero crossing occurs at the same location, approximately 20°, for both the Zoeppritz and Spratt reflection coefficients. The Spratt approximation exhibits very similar behavior as the full Zoeppritz reflection coefficient over a large range of incidence angles, but it varies somewhat from the full Zoeppritz reflection coefficient values approaching 40° incidence angle.

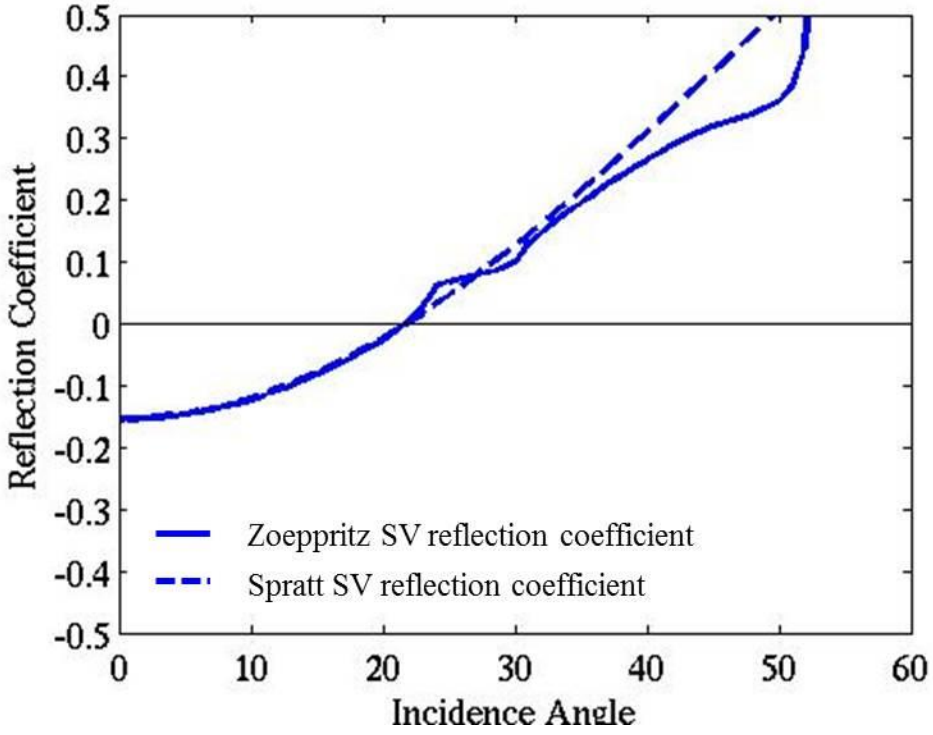

Figure 2.4: Zoeppritz (solid) and Spratt approximation (dashed) reflection coefficients for an SV wave incident on an interface with medium properties described in Table 2.1. The zero crossing occurs at the same location, approximately 20°, for both the Zoeppritz and Spratt reflection coefficients. The Spratt approximation exhibits very similar behavior as the full Zoeppritz reflection coefficient over a large range of incidence angles, only differing somewhat beyond 30° incidence angle.

Lyons (2006) proposed a similar approximation for SH-wave reflection coefficients:

$$\hat{S}\acute{S}_{SH} = -R_S + \frac{1}{2}\frac{\Delta\beta}{\bar{\beta}} tan^2\theta \ . \qquad 2.13$$

Similar to the expression for SV-reflectivity, this approximation can be decomposed into terms that represent near- and far-offset contributions:

$$\grave{S}\acute{S}_{SH} = A + Btan^2\theta \ , \qquad 2.14$$

where

$$A = -R_S \qquad 2.15$$

controls near-offset reflectivity and

$$B = \frac{1}{2}\frac{\Delta\beta}{\bar{\beta}} \qquad 2.16$$

controls far-offset reflectivity. Figure 2.5 shows Zoeppritz (solid) and Lyons (dashed) reflection coefficients for an SH wave incident on an interface. The red lines are calculated using medium properties described in Table 2.1. The blue and black lines are calculated with incremental decreases in shear wave velocity contrast across the interface. For all models, the Lyons approximation provides a very close fit to the true Zoeppritz equations up to about 30° incidence angle. The Lyons approximation provides a closer fit to the original Zoeppritz equations to increasingly larger incidence angles as the shear wave velocity contrast across the reflection interface decreases. For the blue line, there is sufficient agreement between the original Zoeppritz equations and the Lyons approximation up to 35° incidence angle. For the black line, representing the smallest contrast in shear wave velocity, the Lyons approximation provides an excellent fit to incidence angles as large as 55°. However, for large shear wave velocity contrasts, modeled with the red line and calculated with properties in Table 2.1, the agreement is poor beyond 30° incidence angle. The zero crossing locations of the red lines occur at 42° incidence angle when using the original Zoeppritz equations and at 50° incidence angle when using the Lyons approximation. As the shear wave velocity contrast across the interface decreases, the zero crossing locations converge. The zero crossing locations of the blue lines occur at about 47° incidence angle when using the original Zoeppritz equations and at about 52° incidence angle when using the Lyons approximation. The zero crossing location of the black lines, representing the smallest shear wave velocity contrast, occur at about 57° incidence angle when using the original Zoeppritz equations and at about 59° incidence angle when using the Lyons approximation

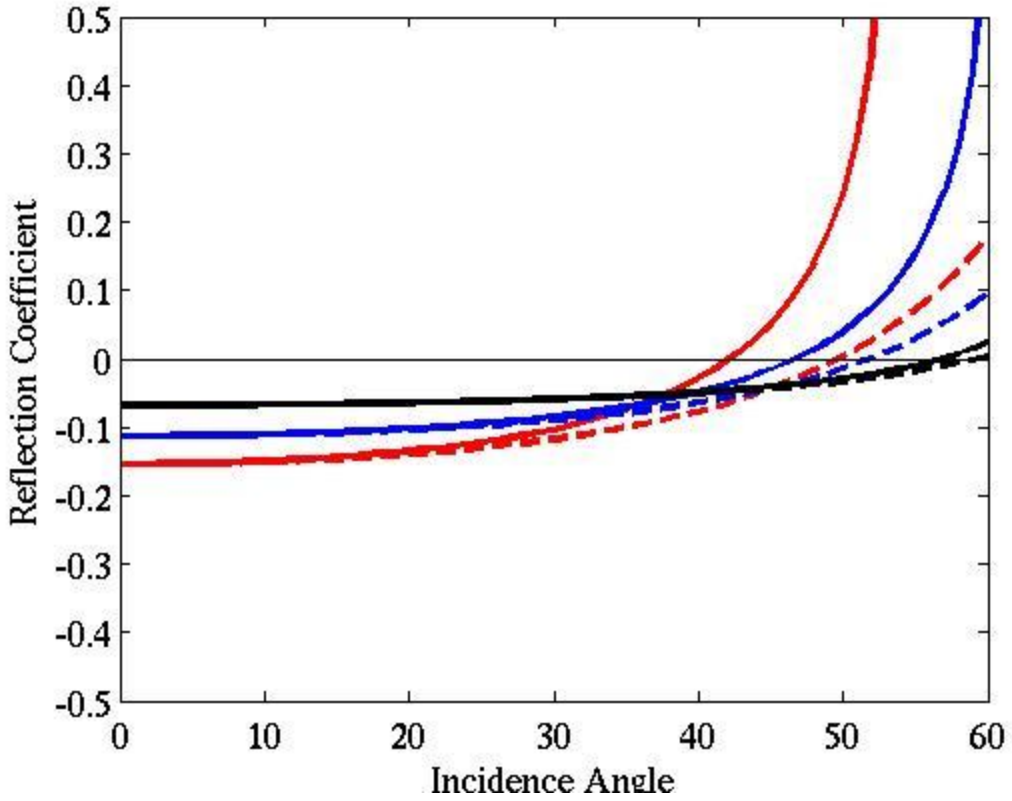

Figure 2.5: Zoeppritz (solid) and Lyons (dashed) reflection coefficients for an SH wave incident on an interface with medium properties described in Table 2.1. The Lyons approximation provides a very close fit to the true Zoeppritz equations up to about 30° incidence angle for all models, but agreement between the Lyons and Zoeppritz calculations deteriorates beyond 30° incidence angle. As the shear wave velocity contrast across the interface decreases, the Lyons approximation provides an increasingly improved fit to the original Zoeppritz equations and the location of respective zero crossings converge.

The Spratt et al. (1993) and Lyons (2006) approximations provide a sufficient fit to the original Zoeppritz equations. Because of their intuitive simplicity, they will be employed in polarization corrections later presented in the discussion of methods in Chapter 3.

2.1.3 Implications for shear wave polarization

Shear wave reflection coefficient behavior at non-normal incidence angles has significant implications for polarization analysis. At near-vertical incidence, reflected shear-wave polarizations are equal to the source polarization. As offset increases, however, reflected shear-wave polarization begins to deviate from the original source polarization. For example, Crampin (1985) notes that phase distortion of 180°, or a phase reversal, arises from and corresponds to the zero crossings of each shear mode's reflection coefficient. The SV polarity reversal typically occurs near an incidence angle of approximately 20° (24° in Figure 2.4). SV polarizations become increasingly distorted and SV amplitudes decrease significantly in strength as incidence angles approach the point of the polarity reversal. At 15° incidence angle, the SV reflection coefficient in Figure 2.4 is almost half the value observed at normal incidence. SH-wave polarizations, on the other hand, do not exhibit significant polarization distortion until much larger offsets. SH-wave reflection coefficient values remain fairly constant up to incidence angles of about 20°. Beyond 20° incidence angle, SH-wave reflection coefficient values begin to decrease by as much as half the normal incidence value at 35° as they approach the zero-crossing at 40° incidence angle. SH-wave polarization distortion, therefore, becomes significant beyond 30° incidence angle, and continues as such through and beyond the angle of the zero-crossing. SH-wave polarization distortion does not present as large of a concern as SV-polarization distortion because data beyond 30° incidence

angle is rarely available for analysis. Further, due to the differences in SV and SH reflectivity (Campbell, 2013) significant polarization distortion at relatively modest offsets is also noted. This leads to changes in the polarization of the reflected shear wave other than a simple phase change.

To illustrate these shear-wave polarization effects, consider a typical 3D direct shear survey with the geometry shown in Figure 2.6. The x-axis of the acquisition grid is defined as 0°, and angles increase in a counter-clockwise direction. The source is located at the origin, in the center of the aerial distribution of receivers. Maximum offset along each axis is 2000 m. Angles ψ and ϕ are the source polarization and source-receiver azimuth, respectively. $\boldsymbol{P}$ is the actual polarization of the reflected shear wave, i.e. the particle motion detected at the receiver. SV and SH are the vertically and horizontally polarized components of reflectivity. For an isotropic medium described in Table 2.2, reflection polarization, $\boldsymbol{P}$, can be estimated based on the geometry presented in Figure 2.6.

$$\boldsymbol{P} = \begin{cases} arctan\left[\frac{\cos(\phi-\psi)SV}{sin(\phi-\psi)SH}\right] + (\phi - 90) & \phi > \psi \\ arctan\left[\frac{\cos(\phi-\psi)SV}{sin(\phi-\psi)SH}\right] + (\phi + 90) & \phi < \psi \end{cases} \qquad 2.17$$

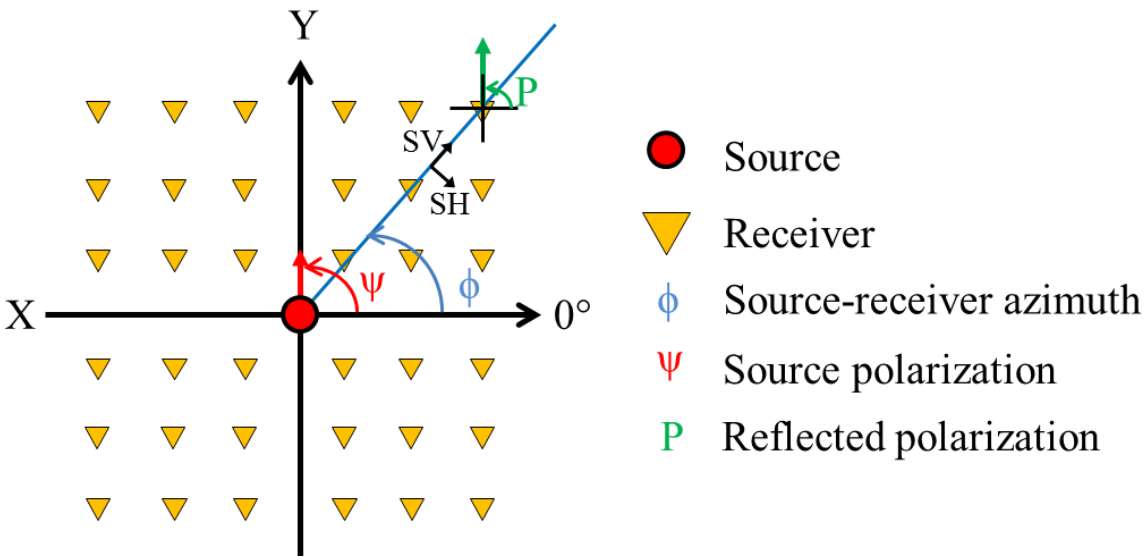

Figure 2.6: Schematic of a 3D survey geometry with a multicomponent source and multi-component receivers. Positive source-receiver angles (ϕ) are measured counterclockwise. For an x-oriented source, ψ =0° or a y-oriented source, ψ =90° (ψ is the source polarization). **P** shows the observed polarization of the reflected shear wave, which is recorded on both the x and y horizontal receiver components.

	V_P (m/s)	V_S (m/s)	Density (g/cm^3)	Thickness (m)
Layer 1	3000	1500	2.0	2000
Layer 2	4000	2000	2.2	half space

Table 2.2: Isotropic model properties used to demonstrate polarization distortion upon reflection.

Figure 2.7 shows a map view of polarizations of the reflected shear wave for a single-shear-source oriented due east (orange arrow), for a reflection from an interface between two isotropic media described in Table 2.2. Maximum offset along each axis is 4000 m. Reflector depth is at 2000 m. The length and orientation of each vector indicates the amplitude and polarization, respectively, of the reflected shear wave calculated from

Zoeppritz reflection coefficients. A blue dashed circle denotes the offset at which reflections incident upon the reflector at 20° are recorded. Within the blue dashed circle, reflected polarizations are consistent with the source polarization. From 0°-24°, the SV and SH reflection coefficients are negative, and reflected polarizations pictured in Figure 2.7 point in the opposite direction of the source polarization. Outside of the blue dashed circle, reflected shear wave polarizations become increasingly distorted, varying from the source polarization by up to 180°. This corresponds to the SV polarity reversal that was observed at 24° in computed reflectivity curves of Figure 2.2. A red dashed circle denotes the offset that corresponds to reflections recorded from an incidence angle of 40°. Reflected polarizations again show erratic behavior, varying by up to 180° across the red dashed circle. This corresponds to the SH polarity reversal that was observed at 40° in computed reflectivity curves of Figure 2.2.

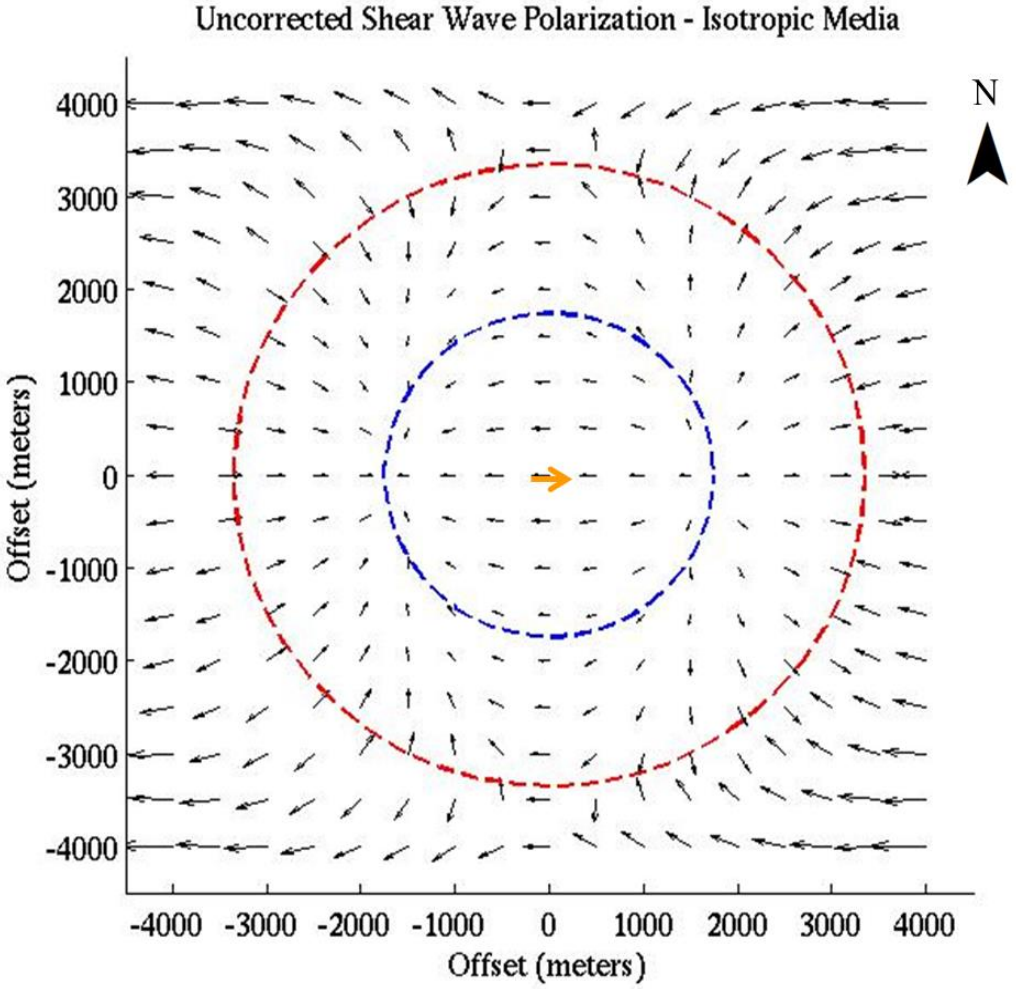

Figure 2.7: Map view of reflected polarizations for a single shear-source oriented due east (orange arrow) for isotropic media with properties defined in Table 2.2. Maximum offset along each axis is 4000 m, and reflector depth is at 2000 m. The length and orientation of each vector indicates the amplitude and polarization, respectively, of the reflected shear wave. Note that as offset increases, reflected polarizations become increasingly distorted. Both the SV and SH polarity reversals can be observed at approximately 20° and 40° and are denoted by blue and red dashed lines, respectively. Adapted from Campbell and Tatham (2013).

2.2 SHEAR WAVES IN ANISOTROPIC MEDIA

2.2.1 Anisotropic symmetry systems

A medium that is transversely isotropic has a single axis of rotational symmetry. A vertically transverse isotropic (VTI) medium has a vertical axis of symmetry (Figure 2.8). Any layered media inherently possesses VTI properties. Common geologic causes of VTI include large-scale sedimentary layering and fine-scale sedimentary laminations, aligned rock fabrics due to depositional setting, and preferred mineral orientations, often observed with flat clay platelets. The stiffness matrix of VTI media can be represented with five independent stiffnesses:

$$c^{(VTI)} = \begin{pmatrix} c_{11} & c_{11}-2c_{66} & c_{13} & 0 & 0 & 0 \\ c_{11}-2c_{66} & c_{11} & c_{13} & 0 & 0 & 0 \\ c_{13} & c_{13} & c_{33} & 0 & 0 & 0 \\ 0 & 0 & 0 & c_{55} & 0 & 0 \\ 0 & 0 & 0 & 0 & c_{55} & 0 \\ 0 & 0 & 0 & 0 & 0 & c_{66} \end{pmatrix}. \qquad 2.18$$

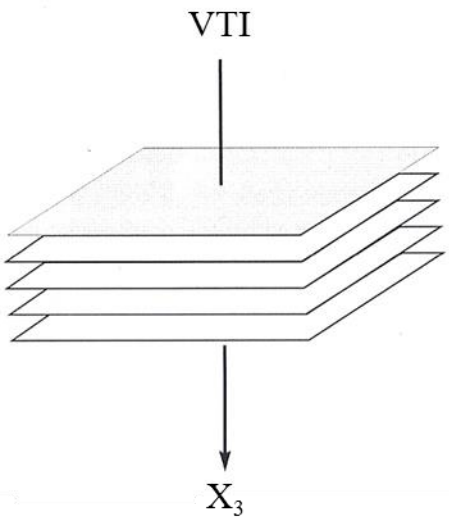

Figure 2.8: Vertical transverse isotropy (VTI) has a vertical axis of symmetry. This representation is useful when describing geologic characteristics such as large-scale sedimentary layering and fine-scale sedimentary laminations, aligned rock fabrics due to depositional setting, and preferred mineral orientations, often observed with flat clay platelets. VTI has a first order effect on seismic velocity. The velocity of a seismic wave in VTI media will vary depending upon the angle between the symmetry axis and the direction the wave is propagating.

Thomsen (1986) recognized the prevalence of anisotropy among sedimentary rocks and its implications for wave propagation. Motivated by the difficulty of expressing the magnitude of anisotropy and its effect on the seismic response in c_{ij} notation, Thomsen proposed the use of the following dimensionless parameters for VTI media:

$$\epsilon = \frac{c_{11}-c_{33}}{2c_{33}} \tag{2.19}$$

$$\gamma = \frac{c_{66}-c_{55}}{2c_{55}} \tag{2.20}$$

$$\delta = \frac{(c_{13}+c_{55})^2-(c_{33}-c_{55})^2}{2c_{33}(c_{33}-c_{55})}. \quad 2.21$$

The velocity of a seismic wave can be directly related to specific coefficients in the stiffness matrix. Velocity of a vertically travelling P- and S- wave can therefore also be represented using two independent stiffness coefficients:

$$V_{P0} = \sqrt{\frac{c_{33}}{\rho}} \quad 2.22$$

$$V_{S0} = \sqrt{\frac{c_{55}}{\rho}}. \quad 2.23$$

If the symmetry axis is rotated 90° to lie within the horizontal plane, the medium becomes a horizontally transverse isotropic medium (HTI) (Figure 2.9). HTI commonly manifests as azimuthal anisotropy in geologic contexts. Vertical, aligned, cracks, fractures, and subsurface stresses are common causes of azimuthal anisotropy and are prevalent among many exploration targets. With proper indicial substitution, the stiffness matrix for HTI media can likewise be represented with five independent stiffnesses:

$$c^{(HTI)} = \begin{pmatrix} c_{11} & c_{13} & c_{13} & 0 & 0 & 0 \\ c_{13} & c_{33} & c_{33}-2c_{44} & 0 & 0 & 0 \\ c_{13} & c_{33}-2c_{44} & c_{33} & 0 & 0 & 0 \\ 0 & 0 & 0 & c_{44} & 0 & 0 \\ 0 & 0 & 0 & 0 & c_{55} & 0 \\ 0 & 0 & 0 & 0 & 0 & c_{55} \end{pmatrix}. \quad 2.24$$

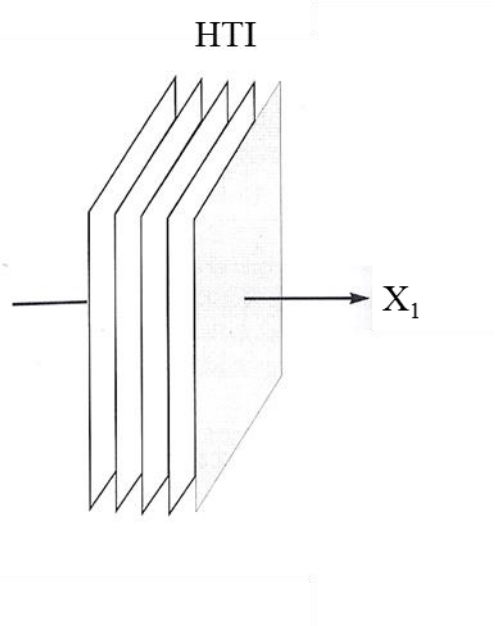

Figure 2.9: HTI media has a horizontal axis of symmetry. HTI commonly manifests as azimuthal anisotropy in geologic contexts, which may be caused by vertical, aligned, cracks, fractures, or subsurface stresses. Seismic velocities are directly related to coefficients in the stiffness matrix, and HTI thus has a first order effect on seismic velocities. This direct relation causes the velocity of the seismic wave to vary according to the angle between the symmetry axis and the direction the wave is propagating.

Thomsen's parameters for VTI media can be represented in an equivalent manner for HTI media using proper indicial substitution. Thomsen's parameters, defined with respect to the vertical for HTI media are:

$$\epsilon^{(V)} = \frac{c_{11}-c_{33}}{2c_{33}} \qquad 2.25$$

$$\gamma^{(V)} = \frac{c_{66}-c_{44}}{2c_{44}} \qquad 2.26$$

$$\delta^{(V)} = \frac{(c_{13}+c_{55})^2-(c_{33}-c_{55})^2}{2c_{33}(c_{33}-c_{55})}. \quad 2.27$$

Seismic velocities of vertically travelling P- and S- waves can again be represented using specific coefficients in the stiffness matrix. Two S-wave velocities are necessary to describe waves polarized parallel and perpendicular to the isotropy plane.

$$V_{P0} = \sqrt{\frac{c_{33}}{\rho}} \quad 2.28$$

$$V_{S0}^{\perp} = \sqrt{\frac{c_{55}}{\rho}} \quad 2.29$$

$$V_{S0}^{\parallel} = \sqrt{\frac{c_{44}}{\rho}} \quad 2.30$$

Seismic velocities in anisotropic media vary according to their direction of propagation. A P-wave propagating at any direction within the isotropy plane will travel at the same velocity for any direction contained within the isotropy plane. A P-wave propagating within the isotropy plane does, however, travel faster than a P-wave propagating along the symmetry axis or at any path that is not entirely within the isotropy plane. Shear wave velocities also exhibit directional variations within anisotropic media. Shear wave velocities in anisotropic media depend not only on the direction of propagation, but the direction of polarization as well. For propagation within the isotropy plane, shear waves that are polarized parallel to the isotropy plane travel faster than shear waves that are polarized perpendicular to the isotropy plane (i.e. parallel to the symmetry axis). For propagation along the symmetry axis, all transverse polarizations are contained

within the isotropy plane, and consequently, shear wave velocity does not depend on the direction in which the wave is polarized. Cumulatively, a shear wave propagating within the isotropy plane travels faster than a shear wave propagating along the symmetry axis. White (1983) provides phase velocities of P-, SV-, and SH-wave modes as a function of phase angle, θ, measured from the vertical symmetry axis and five independent stiffness coefficients:

$$2\rho V_P^2 = (c_{11} + c_{55})\sin^2\theta + (c_{33} + c_{55})\cos^2\theta + K \quad 2.31$$

$$2\rho V_{SV}^2 = (c_{11} + c_{55})\sin^2\theta + (c_{33} + c_{55})\cos^2\theta - K \quad 2.32$$

$$\rho V_{SV}^2 = c_{66}\sin^2\theta + c_{55}\cos^2\theta \quad 2.33$$

where

$$K = \sqrt{((c_{11} - c_{55})\sin^2\theta - (c_{33} - c_{55})\cos^2\theta)^2 + 4(c_{13} + c_{55})^2\sin^2\theta\cos^2\theta}. \quad 2.34$$

Expressing seismic velocities as a function of stiffness coefficients, as in equations 2.31, 2.32, and 2.33, are convenient for numerical computations, but are not easily adapted to analysis of surface seismic data. Independent stiffness coefficients cannot be readily extracted or interpreted from seismic data, making it difficult to understand the magnitude of anisotropy and its effects on the seismic response. It is much simpler to consider phase velocities near vertical, and Thomsen's parameters, therefore, provide a more intuitive framework to assess the magnitude of anisotropy. ϵ can be physically interpreted as the fractional difference between the horizontal and vertical P-

wave velocity. γ is the fractional difference between the velocities of SH-waves propagating the fast and slow (horizontal and vertical) SH-wave velocity. δ, which arguably has a less intuitive meaning, is a measure of variation in P-wave velocity with phase angle for near vertical propagation. Average values for ϵ, γ, δ are not well constrained. Thomsen (1986) reports a "silty limestone" with ϵ=0.056, δ=-0.003, and γ=0.067, a pair of "limestone-shales" with a range of ϵ=0.134-0.169, δ=0.000, and a range of γ=0.156-0.271, a "limestone-anisotropic shale" with ϵ=0.169, δ=0.000, and γ=0.271, and a gypsum-weathered material with ϵ=0.1161, δ=-0.140, and γ=0.2781.

2.2.2 Shear wave reflectivity in HTI media

The convenience of Thomsen's parameters has enabled significant advancements in representing and understanding wave propagation in anisotropic media. One particular case of concern to this study is the Ruger (2002) estimation of shear wave reflectivity in HTI media. Considering a 2D survey carried out on a profile along the fracture strike (i.e. within the isotropy plane shown in Figure 2.10), the velocity of the $S^{\parallel}$-wave propagating within the fracture plane with polarization within the plane (SV) can be expressed as

$$\beta^{\parallel} = \sqrt{\frac{c_{44}}{\rho}}, \tag{2.35}$$

and the velocity of the $S^{\perp}$-wave propagating with polarization normal to the plane of propagation within the fracture plane (SH) can be expressed as

$$\beta^{\perp} = \sqrt{\frac{c_{55}}{\rho}}. \tag{2.36}$$

Using the previously defined anisotropy parameter, γ, $\beta^{\perp}$ can be expressed in terms of $\beta(=\beta^{\parallel})$:

$$\beta^{\perp} = \frac{\beta}{\sqrt{1-2\gamma}} \approx \beta(1-\gamma) \tag{2.37}$$

$$\frac{\Delta\beta^{\perp}}{\overline{\beta^{\perp}}} \approx \frac{\Delta\beta}{\bar{\beta}} + \gamma_1 - \gamma_2 \tag{2.38}$$

Reflection coefficients for shear-waves traveling in the fracture plane (isotropy plane) can now be expressed as

$$R_{S^{\parallel}}^{strike} = -\frac{1}{2}\frac{\Delta Z_S}{\overline{Z_S}} + \left(\frac{7}{2}\frac{\Delta\beta}{\bar{\beta}} + 2\frac{\Delta\rho}{\bar{\rho}}\right) sin^2 j - \frac{1}{2}\frac{\Delta\beta}{\bar{\beta}} sin^2 j\, tan^2 j \tag{2.39}$$

$$R_{S^{\perp}}^{strike} = -\frac{1}{2}\left(\frac{\Delta Z_S}{\overline{Z_S}} - \Delta\gamma\right) + \frac{1}{2}\left(\frac{\Delta\beta}{\bar{\beta}} - \Delta\gamma\right) tan^2 j \tag{2.40}$$

where β is the fast shear-wave velocity and Z_S is the shear wave impedance ($\beta\rho$) for the vertically incident fast S-wave.

In a similar fashion, reflection coefficients for shear-waves traveling in the symmetry-axis plane,

$$R_{S^{\parallel}}^{sym} = -\frac{1}{2}\frac{\Delta Z^S}{\overline{Z^S}} + \frac{1}{2}\left(\frac{\Delta\beta}{\bar{\beta}} - \Delta\gamma\right) tan^2 j \qquad 2.41$$

$$R_{S^{\perp}}^{sym} = -\frac{1}{2}\left(\frac{\Delta Z^S}{\overline{Z^S}} - \Delta\gamma\right) + \left\{\frac{7}{2}\left(\frac{\Delta\beta}{\bar{\beta}} - \Delta\gamma\right) + 2\frac{\Delta\rho}{\bar{\rho}} + \frac{1}{2}\left(\frac{\bar{\alpha}}{\bar{\beta}}\right)^2 \left(\Delta\epsilon^{(V)} - \Delta\delta^{(V)}\right)\right\} sin^2 j$$

$$-\frac{1}{2}\left(\frac{\Delta\beta}{\bar{\beta}} - \Delta\gamma\right) sin^2 j\, tan^2 j \qquad 2.42$$

where $\epsilon^{(V)}$ and $\delta^{(V)}$ are Thomsen's anisotropy parameters defined with respect to a vertical symmetry axis.

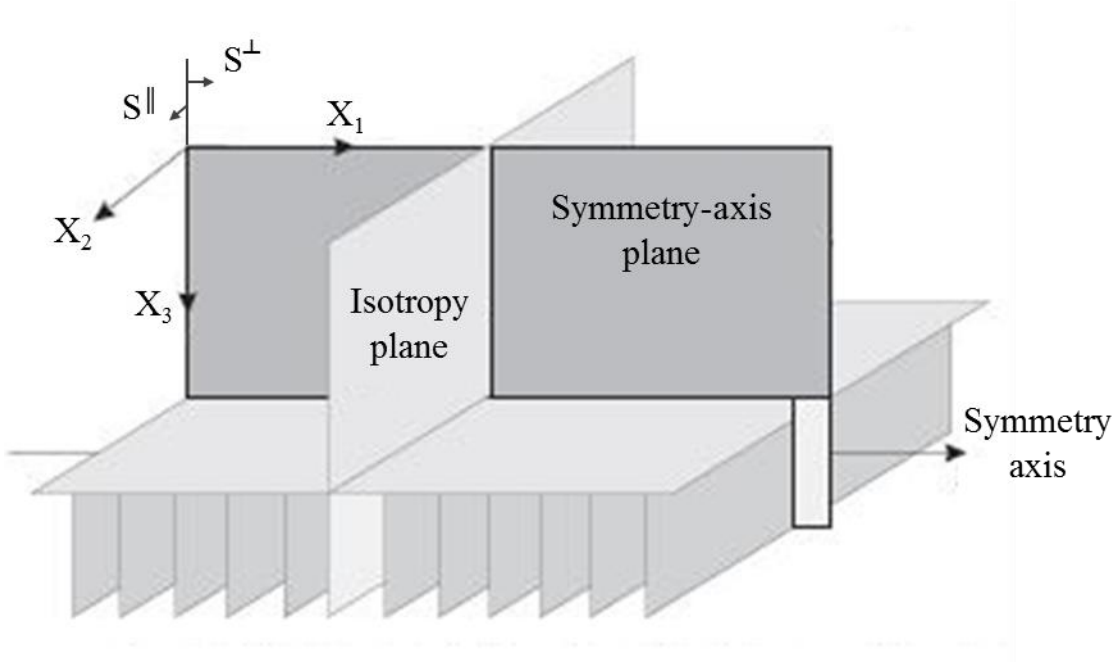

Figure 2.10: Sketch of an HTI model adapted from Ruger (2002) and used in approximations of shear-wave reflectivity in HTI media. Shear waves polarized perpendicular and parallel to the isotropy plane travel at different velocities and require unique representations.

2.2.3 Zero-crossing sensitivity analysis

Figure 2.11 demonstrates the sensitivity of SV and SH zero-crossings to changes in shear wave velocity for reflection coefficients in HTI media calculated using Ruger (2002) approximations. The initial model is defined in Table 2.3 where the shear wave velocity provided is the fast shear wave velocity, and ϵ, δ, and γ are Thomsen's weak anisotropy parameters. Incremental increases and decreases to the interface contrast are introduced by increasing and decreasing the shear wave velocity in layer two, respectively. The zero-crossing remains relatively constant, near 20° for the SV mode. For minimal interface contrasts, the SH mode also remains relatively constant, near 50°. However, as the reflectivity contrast across the interface increases, greater variability

(~4°) can be observed in the SH wave zero-crossing. In this example, all γ values are greater than 10%.

	V_P (m/s)	V_{S1} (m/s)	ρ (kg/m^3)	ϵ	δ	γ
Layer 1	4000	2000	2.2	0.15	0.0	0.14
Layer 2	5000	2500	2.4	0.15	0.0	0.14

Table 2.3: Medium properties used to demonstrate anisotropic zero-crossing sensitivity. Reported shear wave velocity is the fast shear-wave velocity. ϵ, δ, and γ are Thomsen's weak anisotropy parameters.

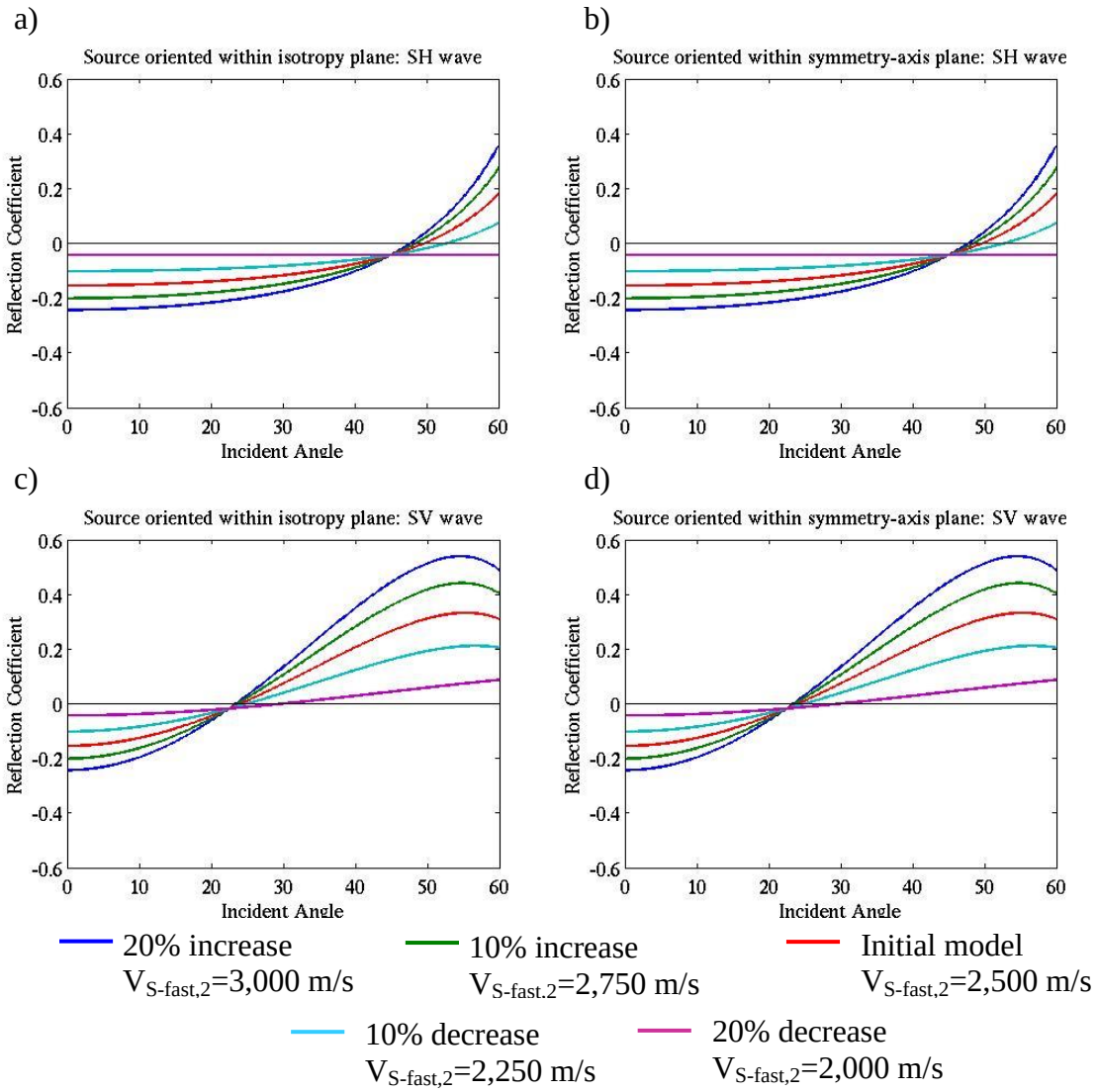

Figure 2.11: Sensitivity of anisotropic reflection coefficient Ruger (2002) zero crossings to shear wave velocity contrasts for an (a) SH wave with a source oriented in the isotropy plane, (b) SH wave with a source oriented in the symmetry-axis plane, (c) SV wave with source oriented in the isotropy plane, and (d) SV wave with source oriented in the symmetry-axis plane. The initial model is described in Table 2.3. Incremental increases and decreases to the interface contrast are introduced by increasing and decreasing the shear wave velocity in layer two, respectively. The zero-crossing remains relatively constant, near 20° for the SV mode and near 54° for the SH mode.

Figure 2.12 demonstrates the sensitivity of SV and SH zero-crossings to changes in shear wave splitting parameter, γ, for reflection coefficients in anisotropic media calculated using Ruger (2002) approximations. The initial model is defined in Table 2.3. Incremental increases and decreases to the interface contrast are introduced by increasing and decreasing the shear wave splitting parameter in layer two, respectively. The SV mode zero-crossing is entirely unaffected by changes in γ, consistently occurring near 20° for all perturbations. The SH mode is minimally affected by changes in γ, not to as large of an extent as was observed for equivalent changes in interface velocity contrast.

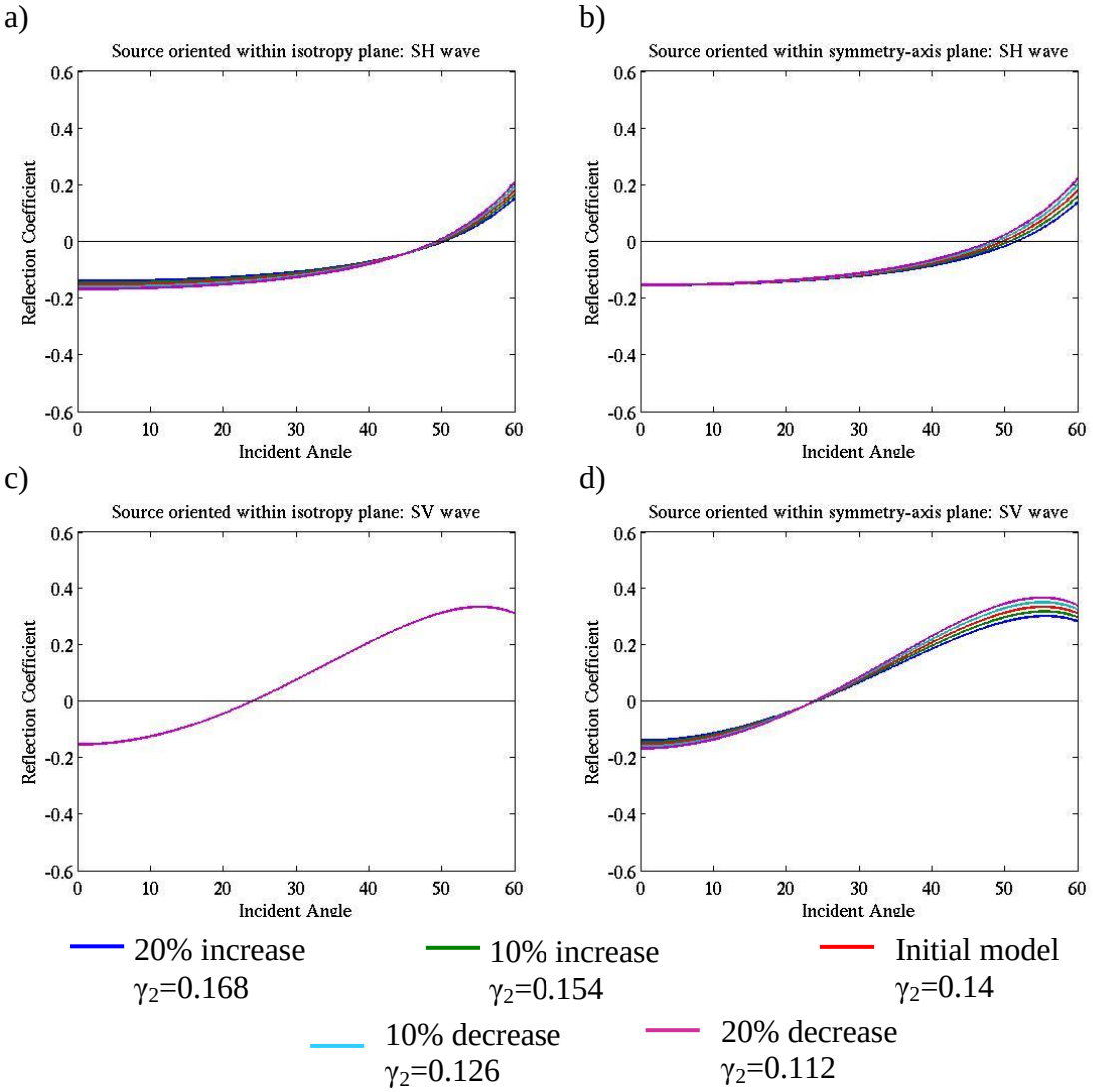

Figure 2.12: Sensitivity of Ruger (2002) anisotropic reflection coefficient zero crossings for an (a) SH wave with a source oriented in the isotropy plane, (b) SH wave with a source oriented in the symmetry-axis plane, (c) SV wave with source oriented in the isotropy plane, and (d) SV wave with source oriented in the symmetry-axis plane. The initial model is described in Table 2.3. Incremental increases and decreases to the interface contrast are introduced by increasing and decreasing the shear wave splitting parameter, γ, in layer two, respectively. The SV-mode zero-crossing is entirely unaffected by changes in γ, occurring at 20° incidence angle for all model perturbations. The SH-mode is minimally affected by changes in γ. All values of γ in this example were greater than 10%.

2.2.4 Shear wave polarizations in anisotropic media

When a shear wave enters an anisotropic medium, shear-wave splitting occurs. As previously discussed, the fast component has particle motion aligned parallel to the isotropy plane, and the slow component has particle motion aligned perpendicular to the isotropy plane. In the case of vertical, aligned cracks or fractures (HTI media), particle motion of arbitrarily polarized SV waves will "split" and align parallel to the isotropy plane (i.e. fracture strike) orientation, which arrives as the fast shear wave. Particle motion of SH waves remains perpendicular to the isotropy plane (i.e., fracture strike) orientation, and arrives as the slow shear wave. Although particle motion of each shear wave component is aligned according the orientation of the anisotropy system of individual layers in the subsurface, polarization distortion is still a key concern. To extract information about the anisotropy characteristics of a layer in the subsurface, the polarizations of the shear waves from shallow layers must be fully understood. That is, reliable polarization information of the waves reflected from the top of the layer must be available to extract the anisotropy parameters of deeper layers.

Chapter 3: Methods

3.1 CORRECTING OFFSET-DEPENDENT SHEAR WAVE POLARIZATION DISTORTION

Lyons (2006) and Campbell and Tatham (2011, 2012, 2013) have shown that offset-dependent shear-wave polarization distortion can be corrected by normalizing amplitudes on individual SV-SV and SH-SH components of non-normal incidence traces to zero offset values. Using the previously discussed approximations for SV- and SH-wave AVO,

$$R_{SV-SV} = A + Bsin^2\theta \tag{3.1}$$

$$R_{SH-SH} = A + Btan^2\theta \tag{3.2}$$

a correction based on incidence angle can be derived for each shear-wave reflection coefficient. Observed amplitudes of reflected SV and SH waves can be divided by the two-term reflection coefficient expressions to minimize post-critical shear-wave polarization distortion. To preserve undistorted near-normal incidence polarization information, however, the value of A must be set to unity.

The B-coefficient can now be estimated for a single known amplitude and incident angle, such as zero-amplitude at the zero-crossing. Lyons (2006) and Campbell and Tatham (2011, 2012, 2013) demonstrated that a uniform zero-crossing exists for both SV and SH reflections under a wide range of density and velocity contrasts. The consistency of SV and SH zero-crossings for anisotropic material was further addressed in Chapter 2. This circumstance is ideal in which to estimate the B-coefficient,

$$0 = 1 + B_{SV} sin^2 j \quad (3.3)$$

$$0 = 1 + B_{SH} tan^2 j \quad (3.4)$$

more simply,

$$B_{SV} = \frac{-1}{sin^2 j} \quad (3.5)$$

$$B_{SH} = \frac{-1}{tan^2 j} \quad (3.6)$$

where *j* is the incident angle at which the zero crossing occurs. Meaningful corrections cannot be applied in the region near angle *j* because the dividing by zero in equations 3.5 and 3.6 introduces instability.

Corrected SV and SH components can now be expressed as

$$R_{SV-corrected} = \frac{R_{SV}}{1+B_{SV} sin^2 \theta} \quad (3.7)$$

$$R_{SH-corrected} = \frac{R_{SH}}{1+B_{SH} tan^2 \theta} \quad (3.8)$$

where R_{SV}-corrected and R_{SH}-corrected are the corrected SV and SH amplitudes, R_{SV} and

R_{SH} are the SV and SH data, B_{SV} and B_{SH} are variables dependent upon SV and SH zero crossings, and θ is incident angle.

Figure 3.1 shows an example of the polarization correction applied to full Zoeppritz SH-SH and SV-SV reflection coefficients for medium properties described in Table 3.1. Where the reflection coefficient reverses polarity, the correction introduces instability and cannot be applied. SH-SH reflectivity exhibits relatively consistent behavior across a large range of incidence angles, up to about 40°. However, due to complex coupled interactions between SV and P modes, the SV-SV reflectivity exhibits unstable behavior across not only the polarity reversal, near a modest 20°, but across the additional critical angle, near 30°, as well. Note, however, that the only information required for this correction is an estimate of the zero-crossing for the pure SV-SV and SH-SH reflectivity. Figure 3.2 shows the polarization correction applied to Ruger (2002) anisotropic reflection coefficients for an SH wave with the source oriented in the isotropy plane (a), an SH wave with the source oriented in the symmetry-axis plane (b), an SV wave with the source oriented in the isotropy plane (c), and an SV wave with the source oriented in the symmetry-axis plane (d). Medium properties are described in Table 3.2 Similar to the isotropic case, the correction cannot be applied within the immediate vicinity of the zero-crossing because it would introduce instability. Nonetheless, the correction is quite successful for the anisotropic case. Once polarization distortions associated with AVA have been removed from all receiver locations associated with a given source position, traditional Alford (1986) rotation analysis can be applied at non-normal angles of incidence.

	V_P (m/s)	V_{S1} (m/s)	ρ (kg/m^3)
Layer 1	4000	2000	2.2
Layer 2	5000	2500	2.4

Table 3.1: Medium properties used to demonstrate the effectiveness of the polarization correction in isotropic media

	V_P (m/s)	V_{S1} (m/s)	ρ (kg/m^3)	ϵ	δ	γ
Layer 1	4000	2000	2.2	0.15	0.0	0.14
Layer 2	5000	2500	2.4	0.15	0.0	0.14

Table 3.2: Medium properties used to demonstrate the effectiveness of the polarization correction at an anisotropic-anisotropic interface. Reported shear wave velocity is the fast shear-wave velocity. ϵ, δ, and γ are Thomsen's weak anisotropy parameters.

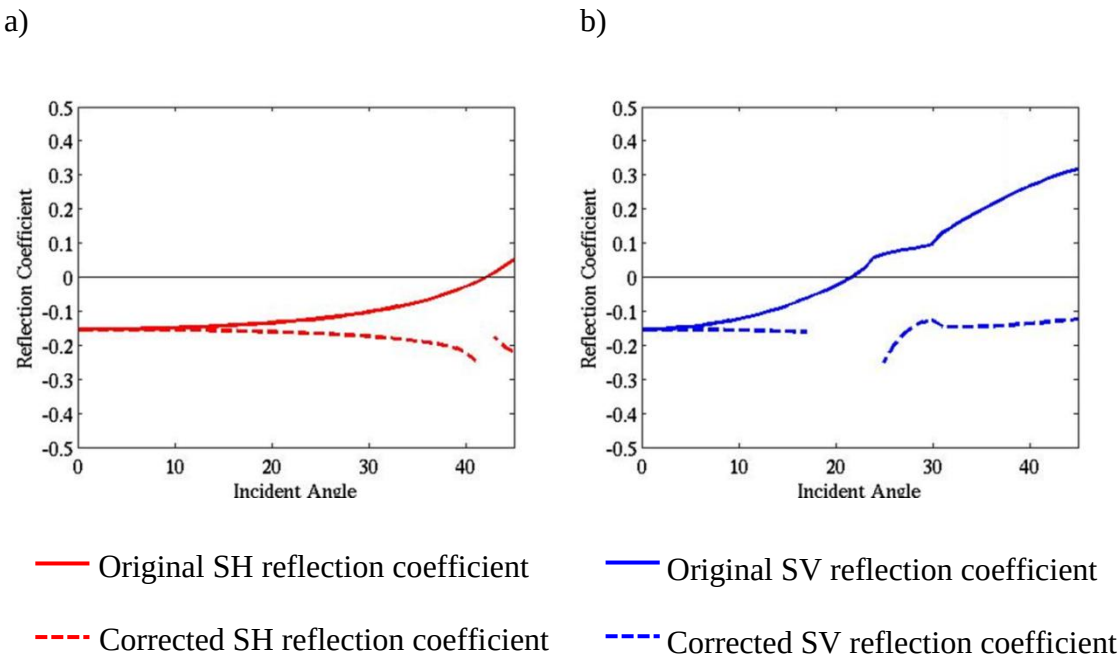

Figure 3.1: Original and corrected Zoeppritz (a) SH and (b) SV reflection coefficients. Where the reflection coefficient reverses polarity, the correction introduces instability and cannot be applied. SH-SH reflectivity exhibits relatively consistent behavior across a large range of incidence angles, up to about 40°. However, due to complex coupled interactions between SV and P modes, the SV-SV reflectivity exhibits unstable behavior across not only the polarity reversal, near a modest 20°, but across the additional critical angle, near 30°, as well. Note that the only information required for this correction is an estimate of the zero-crossing for the pure SV-SV and SH-SH reflectivity.

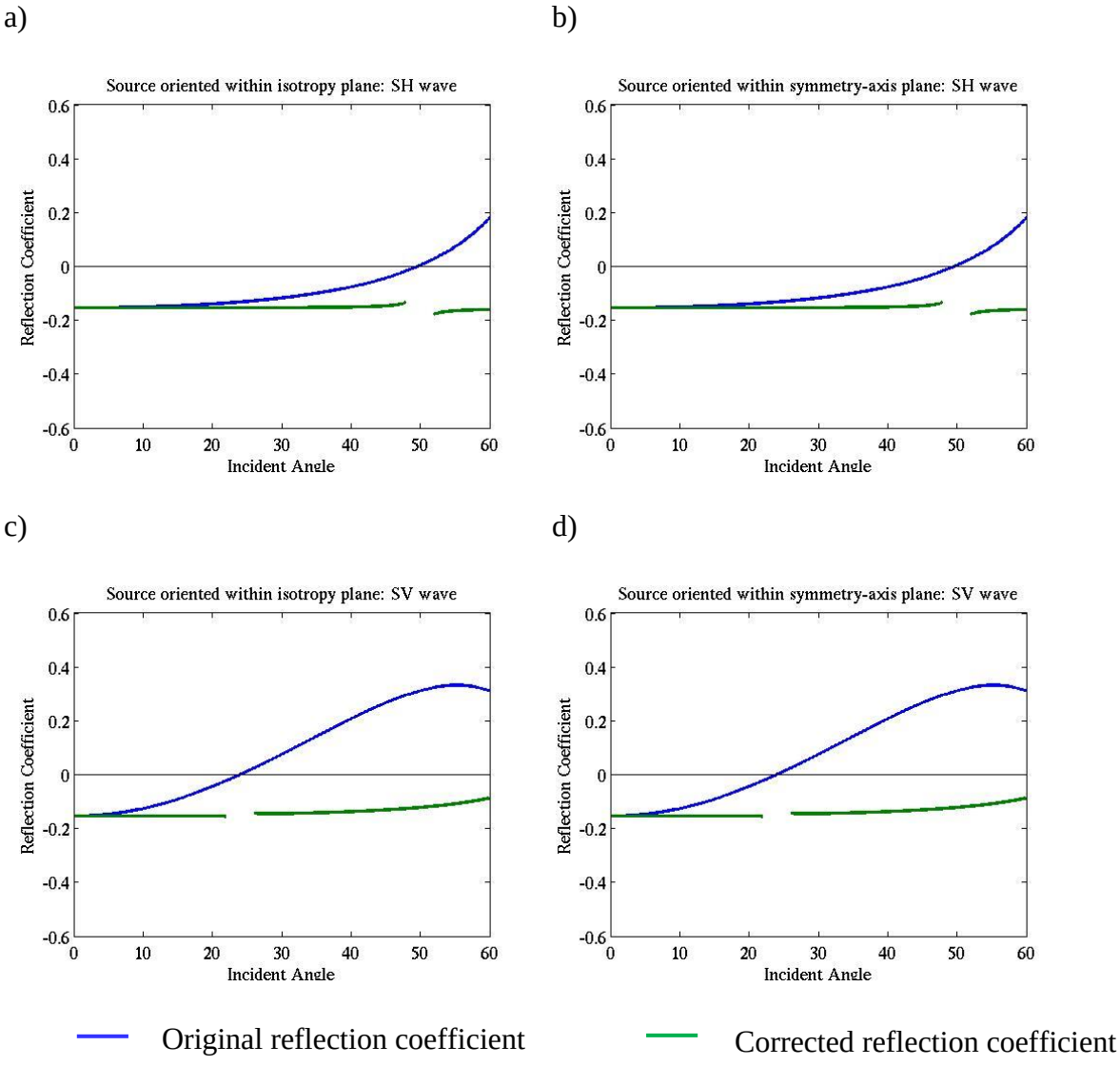

Figure 3.2: Original (blue) and corrected (green) Ruger (2002) anisotropic reflection coefficients for an SH wave with the source oriented in the isotropy plane (a), an SH wave with the source oriented in the symmetry-axis plane (b), an SV wave with the source oriented in the isotropy plane (c), and an SV wave with the source oriented in the symmetry-axis plane (d). Where the reflection coefficient reverses polarity, the correction introduces instability and cannot be applied. Nonetheless, the correction is quite successful for the case of an anisotropic-anisotropic interface.

3.2 ROTATION ANALYSIS

Alford (1986) developed a multi-source/multi-receiver tensor rotation technique to determine the principal direction of anisotropy from shear wave data. This is achieved by computationally rotating source and receiver components to minimize off-diagonal component energy in a 2x2 shear wave data matrix. Considering a 1-D elastic wave generated by a set of orthogonal unit vector sources oriented within the natural isotropy (fracture strike) plane and symmetry-axis plane of an azimuthally anisotropic medium, Alford (1986) describes propagation along the z-axis, perpendicular to the unique axis of an azimuthally anisotropic medium, the matrix notation is

$$\mathbf{E\,U = S\,I,} \qquad \text{Eq. 3.9}$$

where **E** represents the equations of motion, **U** represents the fundamental solutions, **S** represents the source space-time variation, and **I** represents the identity matrix indicating the direction of the sources. **E**, **U**, **S**, and **I** are all 2 x 2 matrices, whose components correspond to source-receiver geometry as follows:

$$\begin{bmatrix} XX & XY \\ YX & YY \end{bmatrix}, \qquad \text{Eq. 3.10}$$

where rows contain the components for the two sources and columns contain the components for the two receivers. X refers to the in-line direction, and Y refers to the

cross-line direction. XX and YY therefore represent acquisition for the in-line source–in-line receiver and cross-line source–cross-line receiver orientations, respectively. Similarly, XY and YX represent acquisition for the cross-line source–in-line receiver and in-line source–cross-line receiver orientations, respectively.

The orientation of azimuthal anisotropy is generally not known prior to data acquisition, or it is difficult to design a survey that conforms to the constructs of mathematical convenience presented above. The acquisition geometry of a 3-D seismic survey alone precludes the simplicity of considering ray paths confined strictly within the isotropy and symmetry-axis planes. It is therefore desirable to find a solution, **V**, for a set of sources and receivers oriented in an arbitrary acquisition system that can be related to the solution, **U**, of the natural anisotropy system by an angle **θ**. This can be achieved by defining an orthogonal rotation matrix,

$$\mathbf{R}(\boldsymbol{\theta}) = \begin{bmatrix} \cos\theta & \sin\theta \\ -\sin\theta & \cos\theta \end{bmatrix}, \qquad \text{Eq. 3.11}$$

which produces a clockwise rotation by the angle **θ** upon left-multiplication with another matrix.

A solution for a set of sources oriented in the acquisition system can now be defined from the solutions for the natural anisotropy system by right multiplying equation 3.9 by **R(θ)**,

$$\mathbf{E\{UR(\theta)\} = SIR(\theta),} \qquad \text{Eq. 3.12}$$

where the term in brackets is the new solution for source components in the natural coordinate system. The new solution, **V**, can be expressed in terms of the acquisition coordinates by

$$\mathbf{ER(\theta)\ \{R^T(\theta)UR(\theta)\} = SR(\theta),} \qquad \text{Eq. 3.13}$$

$$\mathbf{V(\theta) = R^T(\theta)UR(\theta),} \qquad \text{Eq. 3.14}$$

which is equivalent to a clockwise rotation of the natural coordinates through the angle θ. The term in brackets allows field data to be expressed in the simpler solutions associated with the natural anisotropy system. Unsplit solutions can be obtained from **V**, the field data, through a simple inverse to the rotation operation,

$$\mathbf{U = R(\theta)V(\theta)R^T(\theta),} \qquad \text{Eq. 3.15}$$

where the field sources and geophones have been rotated counter-clockwise through the angle θ. The field data has been transformed into the solutions of the natural anisotropy system.

For the purpose of this work, the initial field coordinate system is denoted as the X-Y coordinate frame, composed of X and Y source – receiver pairs, illustrated in Figure

3.3. The post-rotation S-polarization coordinate system is denoted as the X'-Y' coordinate frame. In the isotropic case, the post-rotation coordinate system is composed of radial and transverse source – receiver pairs. In the anisotropic case, the post-rotation coordinate system is composed of fast and slow source – receiver pairs. The angle at which off-diagonal component energy is minimized and diagonal component energy is maximized corresponds to the principal axes of the natural anisotropy system. At this angle, each fast and slow mode arrives as a single event on respective diagonal components.

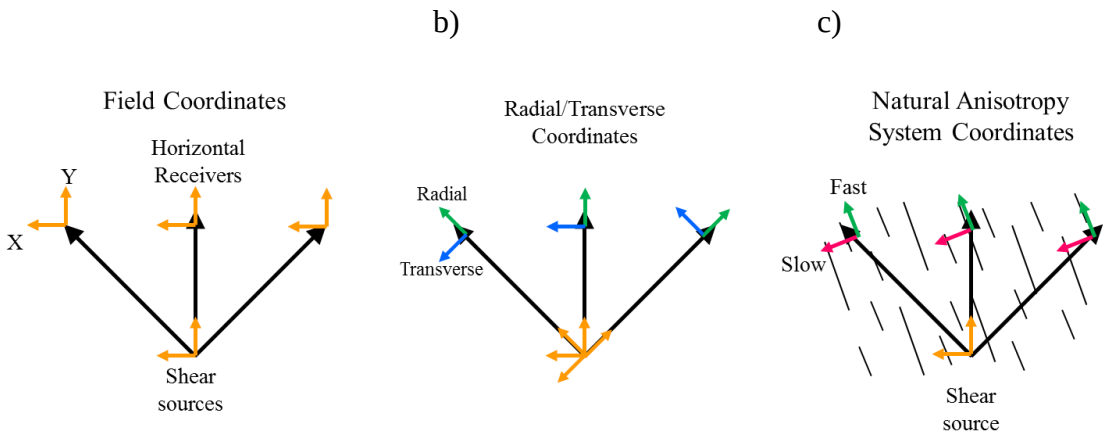

Figure 3.3: Field coordinates expressed as (a) X and Y source – receiver pairs, (b) transformation into radial and transverse coordinates of the survey geometry, and (c) fast and slow coordinates of the natural anisotropy system.

This method allows for the estimation of subsurface fracture orientation, but it is restricted to normal-incidence reflections (Thomsen, 1988). Furthermore, the method assumes a time-invariant rotation angle, which implies a constant polarization angle for all depths. Shear-wave splitting is cumulative, so the presence of depth-variant anisotropy

can complicate rotation analysis unless it is removed. When shear wave polarization changes with depth, the off-diagonal components of the 2x2 S-wave data matrix become distorted and the matrix cannot be diagonalized. Systematic errors in calculated polarization angles will result because the signal on XY components differs from the signal on YX components (Winterstein and Meadows, 1991a).

3.3 LAYER STRIPPING

In order to apply Alford rotation to the case of depth-variant azimuthal anisotropy, a layer-stripping approach must be implemented. The goal of layer-stripping is to transform the reflection traces, as recorded, into a new set of traces that correspond to a purely isotropic overburden. Further, if non-normal incidence angles are to be included in the analysis, corrections to the polarizations of the reflected shear-waves at each interface must also be applied. Layer stripping operates under a number of key assumptions. First, S-wave polarizations are assumed to remain constant within a single layer, generally defined by the anisotropy parameters. Changes in polarization occur discontinuously at layer boundaries, thereby providing a benchmark from which to subtract time lags. Additionally, both layer thickness and the degree of anisotropy must be large enough to cause significant birefringence from which polarization and time lag can be observed. Lastly, it is assumed that wave propagation is along the symmetry axis or plane within each HTI layer. This is necessary for the rotation of sources and receivers by a single angle to adequately diagonalize the 2x2 S-wave matrix (Winterstein and Meadows, 1991a).

Working under the assumptions stated above, layer stripping is performed by first rotating source and receiver axes into alignment with the natural anisotropy system of the uppermost anisotropic layer, defined by the polarization of the fast S-wave. After the data

are transformed into the orientation of the natural anisotropy system, the time delay between the diagonal component fast mode, which has travelled up and down as the fast mode, and slow mode, which has travelled up and down as the slow mode, is removed by shifting traces of the diagonal component slow mode forward in time. Time delays must also be removed from both off-diagonal components (Thomsen et al., 1999). Each off-diagonal arrival has travelled either downward or upward through the anisotropic layer as a fast mode one way and a slow mode the other way and, therefore, arrives with half the time delay of the diagonal component slow mode.

It is then necessary to identify where measurable changes in shear-wave polarization occur, if at all. In practice, polarization directions and any changes in polarization direction are most reliably determined from VSP data (Winterstein and Meadows, 1991a, b). The CVU-200 VSP, acquired in an injection well in the Central Vacuum field, shows two characteristic features that are distinctive of changes in shear-wave polarization with depth. A gradual drift in polarization with depth and abrupt changes in delay time slope are evident in Figure 3.4. The changes in delay time slope serve as an indicator of where shear-wave polarizations are changing and thus where layer stripping needs to be performed.

In seismic data, initial rotations performed on the uppermost layer fail to minimize energy on the X'Y' and Y'X' components beyond depths at which the shear wave polarization changes. Performing additional Alford rotations is necessary, followed by appropriate static time shifts, to minimize off-diagonal component energy in subsequent layers and analyze variations in anisotropy with depth (Winterstein and Meadows, 1991a).

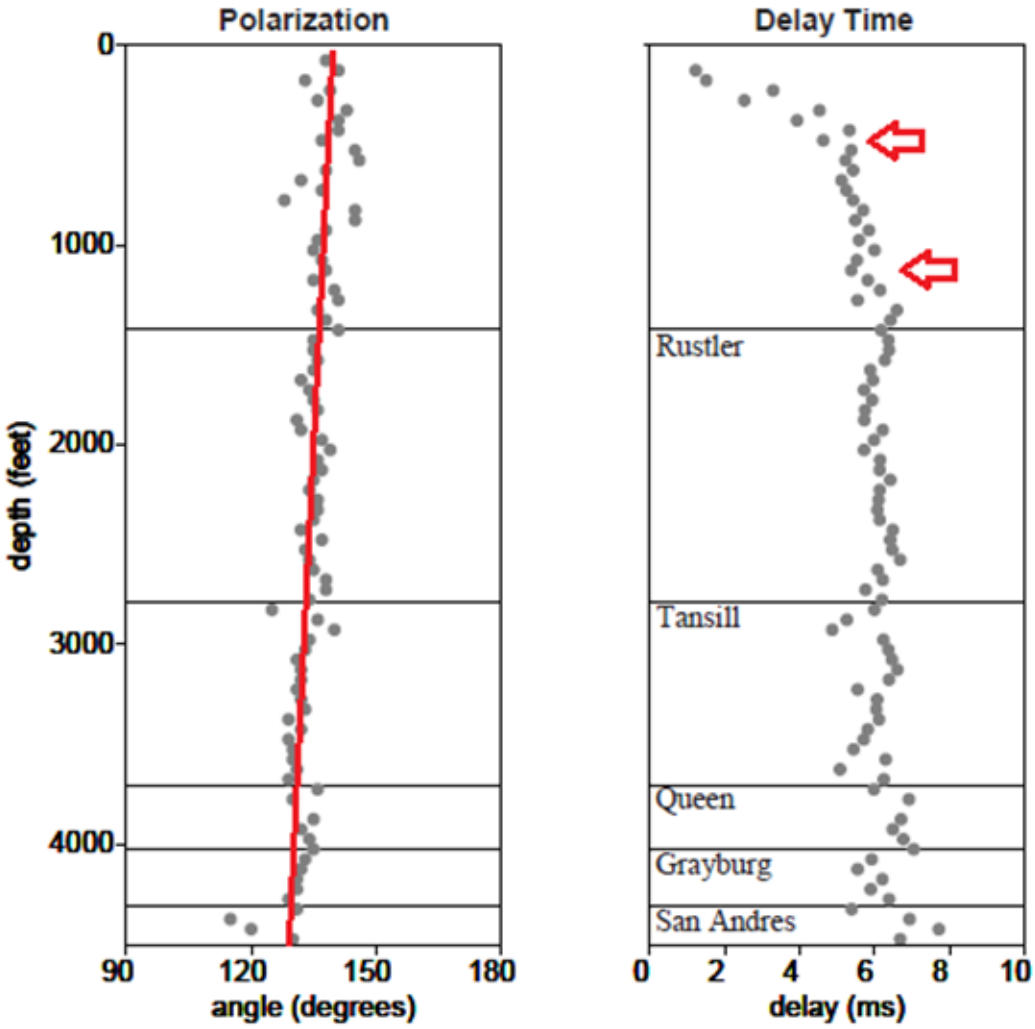

Figure 3.4: Cumulative polarizations and delay times from the CVU-200 vertical seismic profile (VSP) in the Vacuum field from Mattocks (1998). A gradual drift in polarization with depth and abrupt changes in delay time slope serve as an indicator of where shear-wave polarizations are changing and thus where layer stripping needs to be performed.

Chapter 4: Results

4.1 SYNTHETIC DATA

Synthetic 3-D, 9-C data are generated using a Fourier frequency-wave number numerical modeling method (Mallick and Frazer, 1987) for the case in which the orientation of the anisotropy system changes with depth, described in Table 4.1. Thomsen's weak anisotropy parameters are used to describe the anisotropy system and are modeled after values reported at the CVU-200 VSP in Mattocks (1998). The isotropy plane orientation is measured counterclockwise relative to the positive x-axis (0°). The 3D survey geometry used for all synthetic data is shown in Figure 4.1. Maximum offset along each axis is 4000 m, and receivers are spaced 50 m. The source wavelet is a zero-phase Ricker wavelet with a central frequency of 45 Hz. The model source consists of three-components, representing a vertical, radial, and transverse impulse. Each geophone records three-components of motion, resulting in a nine-component record. All primary P- and S-reflections are modeled, including mode-conversions. The direct wave and any P- or S-multiples are not included in the model.

Layer	Thickness (m)	V_P (m/s)	V_S (m/s)	ρ (kg/m^3)	Thomsen parameters	Isotropy plane orientation	Interface
1	1000	2000	1000	2.0	isotropic	-	A
2	1000	3000	1500	2.1	isotropic	-	B
3	1000	4000	2000	2.2	ϵ=0.15 δ=0.0 γ=0.14	60°	C
4	1000	5000	2500	2.4	ϵ=0.15 δ=0.0 γ=0.14	0°	D
5	1000	6000	3000	2.5	isotropic	-	

Table 4.1: Properties of a depth-variant azimuthally anisotropic medium used to model 3D-9C seismic data. Isotropy plane orientation is measured counterclockwise relative to the positive x-axis (0°).

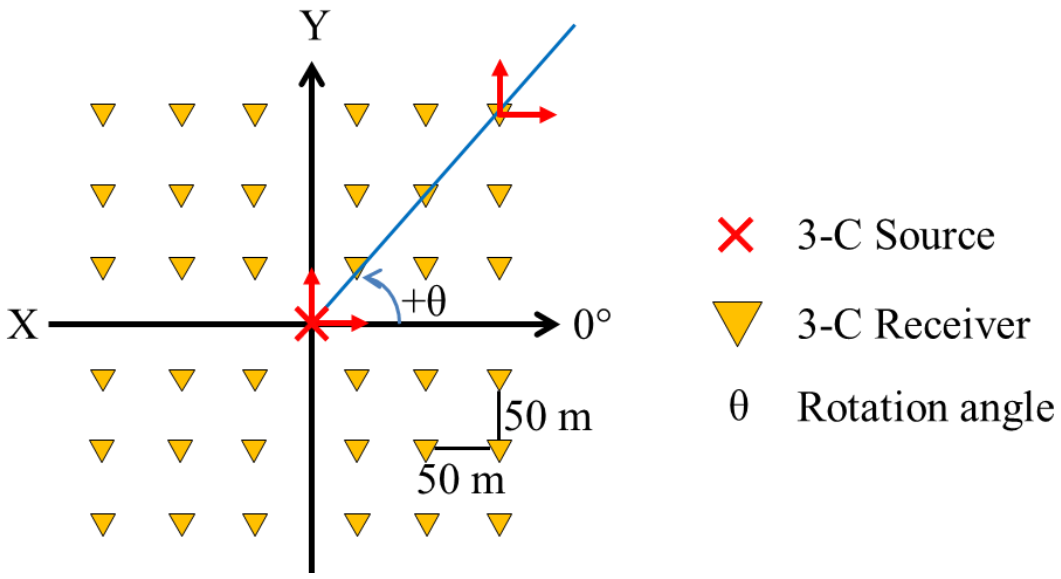

Figure 4.1: Schematic of 3D survey geometry used for all synthetic 9C data. Maximum offset along each axis is 4000 m and receiver spacing is 50 m. Positive angles are measured counterclockwise.

Figure 4.2 shows synthetic shot gathers computed from the model in Table 4.1 for (a) XX, (b) XY, (c) YX, and (d) YY source and receiver components along the x-axis (0°) prior to rotations or polarization corrections. The direct P-wave reflection from the first interface arrives at 1000 ms. This reflection appears strongest on the XX component, does not appear on off-diagonal components, and only appears at middle offsets on the YY component. The PS-mode-converted reflection from the first interface arrives at 1500 ms. Again, this reflection appears strongest on the XX component, does not appear on off-diagonal components, and only appears at middle-to-large offsets on the YY component. The direct shear wave reflection from the first interface (A) an isotropic-isotropic interface, arrives at 2000 ms on the diagonal XX and YY components. This reflection does not appear on the off-diagonal components because inline and crossline sources and receivers are properly oriented in radial and transverse coordinates, and shear-wave splitting does not occur.

Significant energy can be seen on the off-diagonal components for all subsequent direct shear wave reflections (B, C, and D), caused by the presence of anisotropy. The shear wave reflection B arrives at approximately 3300 ms on all four components. This event appears on all four components because the underlying anisotropy system polarizes the incident shear waves into the principal axis directions upon reflection. However, there is no time lag between their arrivals because they have not yet travelled through any anisotropic media.

Similarly, the shear wave reflection from interface C, an anisotropic-anisotropic interface, arrives at approximately 4300 ms on all four components. The source shear wave polarizations have realigned in accordance with the anisotropy system's principal axes and are separated by the time delay accumulated in this layer. The response to the shear wave splitting that occurred in the third layer is mixed among all four components.

Interference between fast and slow modes causes the third interface reflection to arrive as multiple peaks and troughs, rather than a single waveform. The shear wave reflection from the fourth interface (D), an anisotropic-isotropic interface, arrives at approximately 5050 ms in a similar fashion. Recording multiple shear arrivals from a single interface is a defining feature of shear wave splitting and can lead to complicated tuning effects and misguided interpretations if each of the fast and slow shear wave arrivals is not analyzed individually. Furthermore, individual characteristics of SV and SH reflectivity cannot be distinguished because distorted energy from each shear mode is combined on any single component.

Figure 4.3 shows synthetic shot gathers for (a) XX, (b) XY, (c) YX, and (d) YY components for a shot record with a source-receiver angle of 45° prior to rotations or polarization corrections. The same shear wave reflection from the first isotropic-isotropic interface (A) appears on all four components because source and receiver coordinates are misaligned with respect to the source-receiver aazimuth. Subsequent shear wave reflections from the second (B), third (C), and fourth (D) interfaces exhibit similar behavior as observed in Figure 4.2, caused by the presence of azimuthal anisotropy. However, the presence of azimuthal anisotropy cannot be evaluated until receiver coordinates are rotated into alignment with source coordinates and off-diagonal energy from all isotropic-isotropic interfaces is eliminated.

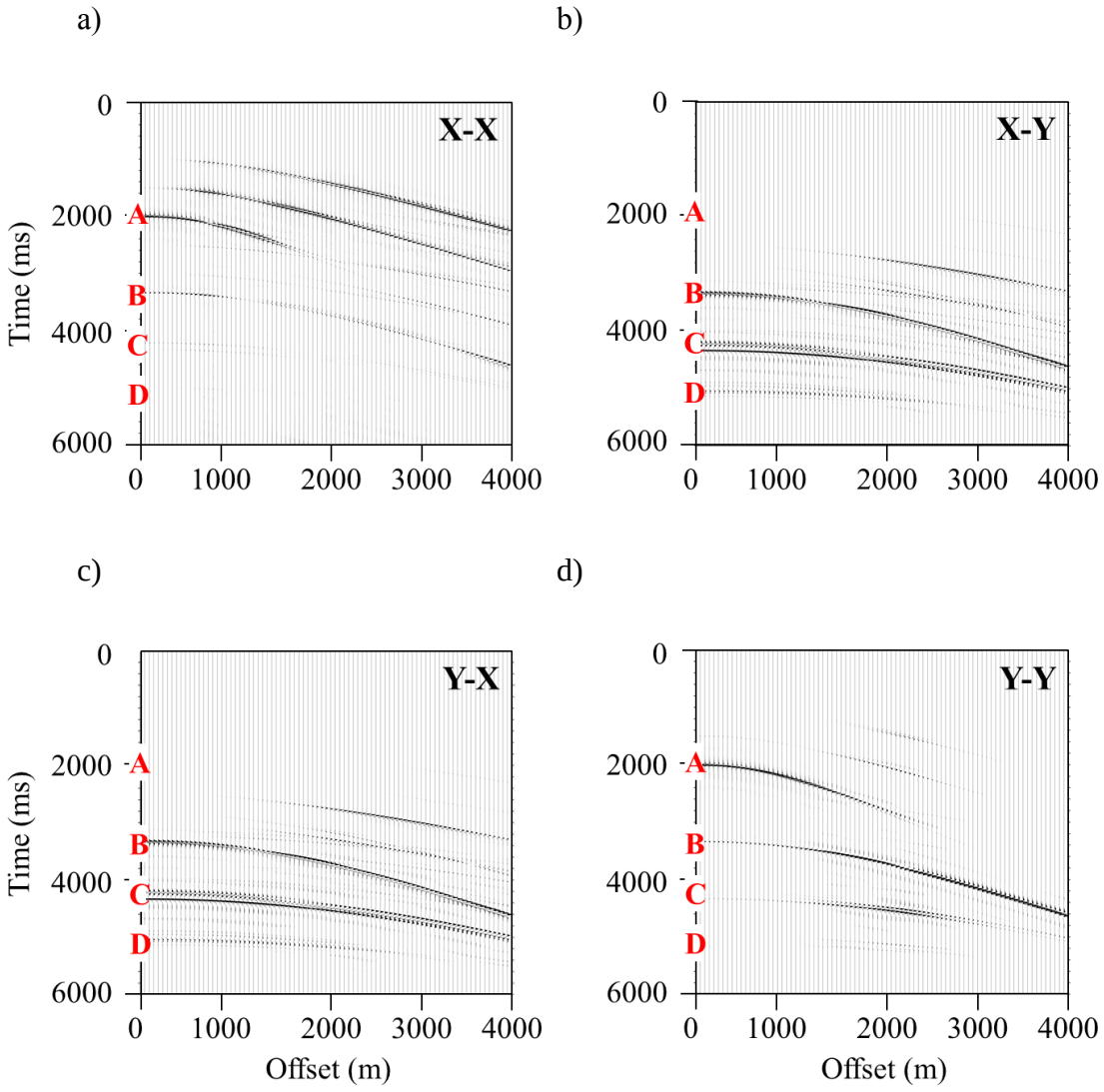

Figure 4.2: Synthetic shot gathers for (a) XX, (b) XY, (c) YX, and (d) YY components along the x-axis (0°) from the five layer model prior to rotations or polarization corrections. The shear wave reflection from the interface A, an isotropic-isotropic interface, does not appear on the off-diagonal components because the source coordinates are aligned with the receiver coordinates. Significant energy can be seen on the off-diagonal components for all subsequent shear wave reflections (B, C, and D), which results from either isotropic-anisotropic or anisotropic-anisotropic interfaces. Individual characteristics of SV and SH reflectivity cannot be distinguished because energy from each shear mode is mixed across all components.

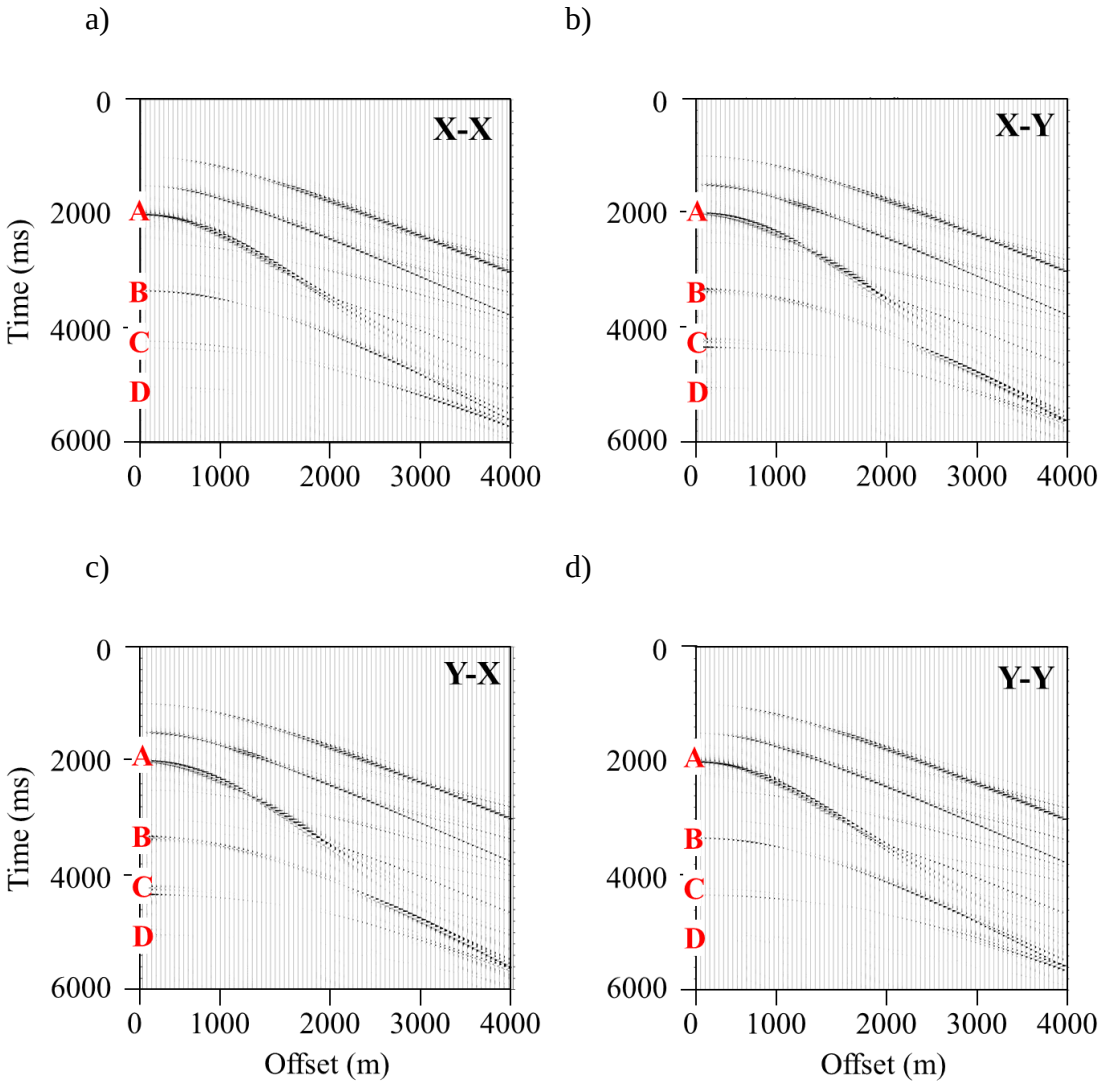

Figure 4.3. Synthetic shot gathers for (a) XX, (b) XY, (c) YX, and (d) YY components for a line at a source-receiver azimuthal angle of 45° prior to rotations or polarization corrections. A shear wave reflection from an isotropic-isotropic interface (A) appears on all components because source and receiver coordinates are misaligned with respect to the source-receiver azimuth. Reflections from azimuthally anisotropic layers (B, C, and D) cannot be evaluated until receiver coordinates are rotated into alignment with source coordinates.

4.2 ROTATION ANALYSIS

The data are incrementally rotated (Alford, 1986) through a range of angles from -90° to 90°. Energy is calculated as an RMS-type average, squaring amplitudes and summing over time windows centered about each flattened reflection and across multiple traces. Energy calculations span a time window from 3324 ms to 3344 ms for the second shear wave reflection (interface B, Figure 4.4), 4100 ms to 4500 ms for the third shear wave reflection (interface C, Figure 4.5), and 4900 ms to 5300 ms for the fourth shear wave reflection (interface D, Figure 4.6). The time window for energy calculations for the second shear wave reflection is smaller than the time window for the third and fourth shear wave reflections because a time delay between each shear wave polarization has not yet accumulated. Energy calculated over a 0° to 5° range of incidence angles includes the ten nearest traces and offsets up to 500 m. A 0° to 10° range of incidence angles includes the twenty nearest traces and offsets up to 1000 m. A 0° to 15° range of incidence angles includes the thirty nearest traces and offsets up to 1500 m. A 0° to 20° range of incidence angles includes the 40 traces and offsets up to 2000 m. The angle at which a maximum ratio of diagonal to off-diagonal component energy is observed corresponds to the orientation of the natural anisotropy system.

Results of rotation analysis performed on the reflection from interface B (Figure 4.4), an isotropic-anisotropic interface, show that energy in off-diagonal component source-receiver pairs is minimized within 5° (near offsets) of the underlying isotropy plane orientation, 60°, and exhibits symmetric behavior about the principal axes. Diagonal component maxima occur at orthogonal rotation angles, approximately -30° on the XX component and 60° on the YY component. However, the distinct off-diagonal component minima successfully maximize the ratio of diagonal to off-diagonal component energy for incidence angles near normal incidence (0°-5°, blue line). This

behavior is consistent with the normal incidence assumptions of traditional Alford rotation. As a larger range of incidence angles are included in the energy calculations, the computed energy maxima and minima drift further from the orientation of the true anisotropy system, illustrating the shortcomings of applying typical Alford rotation at non-normal incidence angles. Although the shear wave has not yet travelled through an anisotropic medium at this point, the underlying anisotropy system polarizes incident shear waves into the principal axis directions upon reflection, as demonstrated in detail by Gumble and Gaiser (2006), and Campbell and Tatham (2012, 2013).

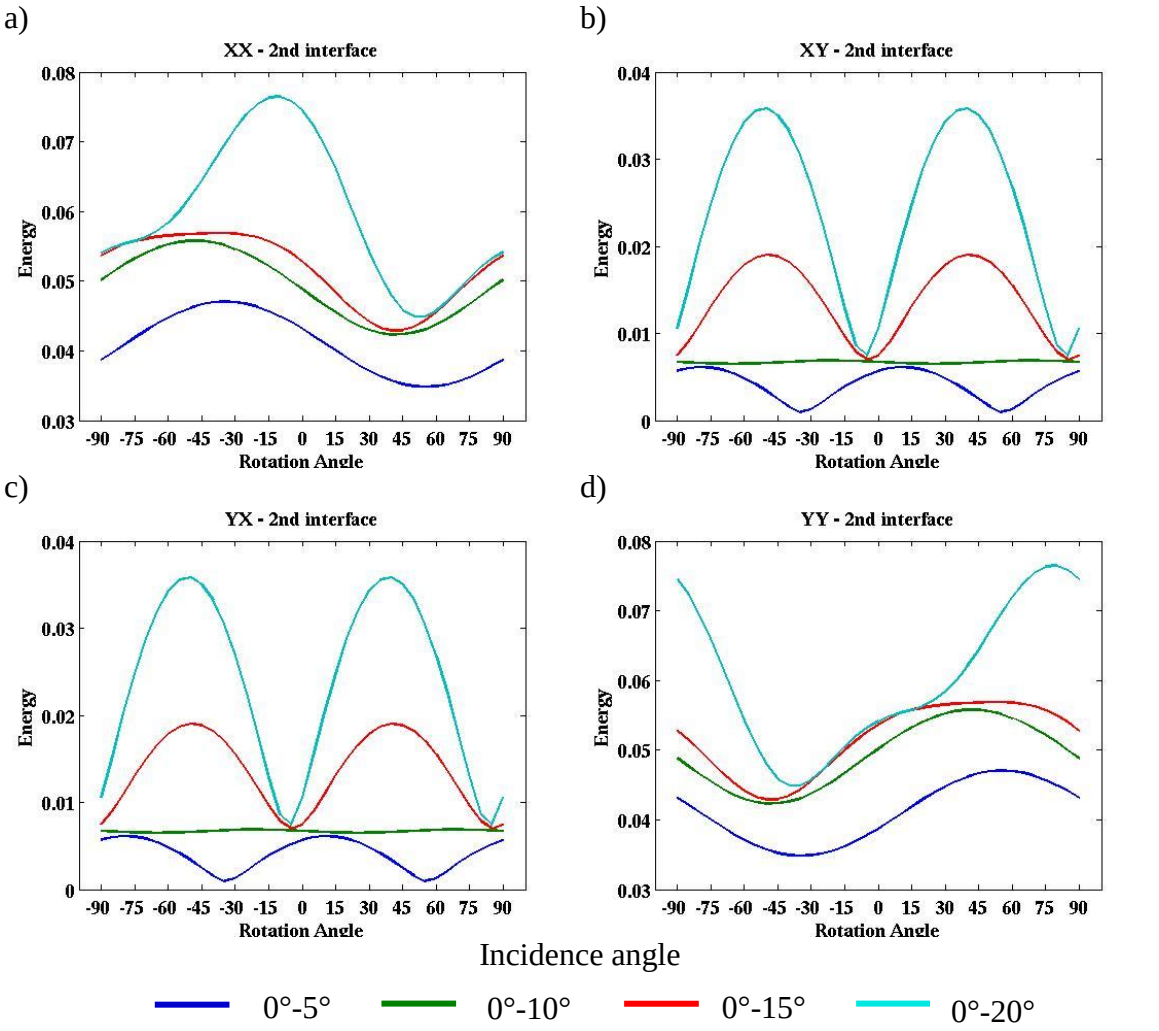

Figure 4.4: Energy calculated on (a) XX, (b) XY, (c) YX, and (d) YY components from the interface B reflection for a range of rotation angles from -90° to 90° and an increasing range of incidence angles. The shear wave has not yet travelled through anisotropic media, but the underlying anisotropy system polarizes shear waves into the principal axis direction (60°) upon reflection. Diagonal component maxima occur at orthogonal rotation angles, approximately -30° on the XX component and 60° on the YY component. Including a greater range of incidence angles causes computed energy maxima and minima to deviate from the true orientation of the natural anisotropy system. This behavior demonstrates the shortcomings of applying current Alford rotation at non-normal incidence angles.

In Figure 4.5, rotation analysis performed on the reflection from interface C, an anisotropic-anisotropic interface, illustrates that energy in off-diagonal component source-receiver pairs is minimized within 5° of the isotropy plane orientation in layer 3, 60°, and again exhibits symmetric behavior about the principal axes. This behavior is consistent with the energy transmitting through the anisotropic layer, with dominant polarization controlled by that layer on transmission. This propagation effect reorients the polarization to the properties of this layer. Absolute maxima occur on diagonal components at orthogonal rotation angles, approximately 60° on the XX component and -30° on the YY component. In comparison to the rotation scan performed on the isotropic-anisotropic interface reflection, one absolute maximum and one smaller, local maximum occur on each diagonal component and result in greater symmetry about the principal axes. A very strong imprint of the transmission through the anisotropic layer is observed. All peaks and troughs in Figure 4.5 show different magnitude, but occur more or less within a few degrees each other. As a larger range of incidence angles are included in the energy calculations the computed energy maxima and minima do show some drift, but not by more than 5°.

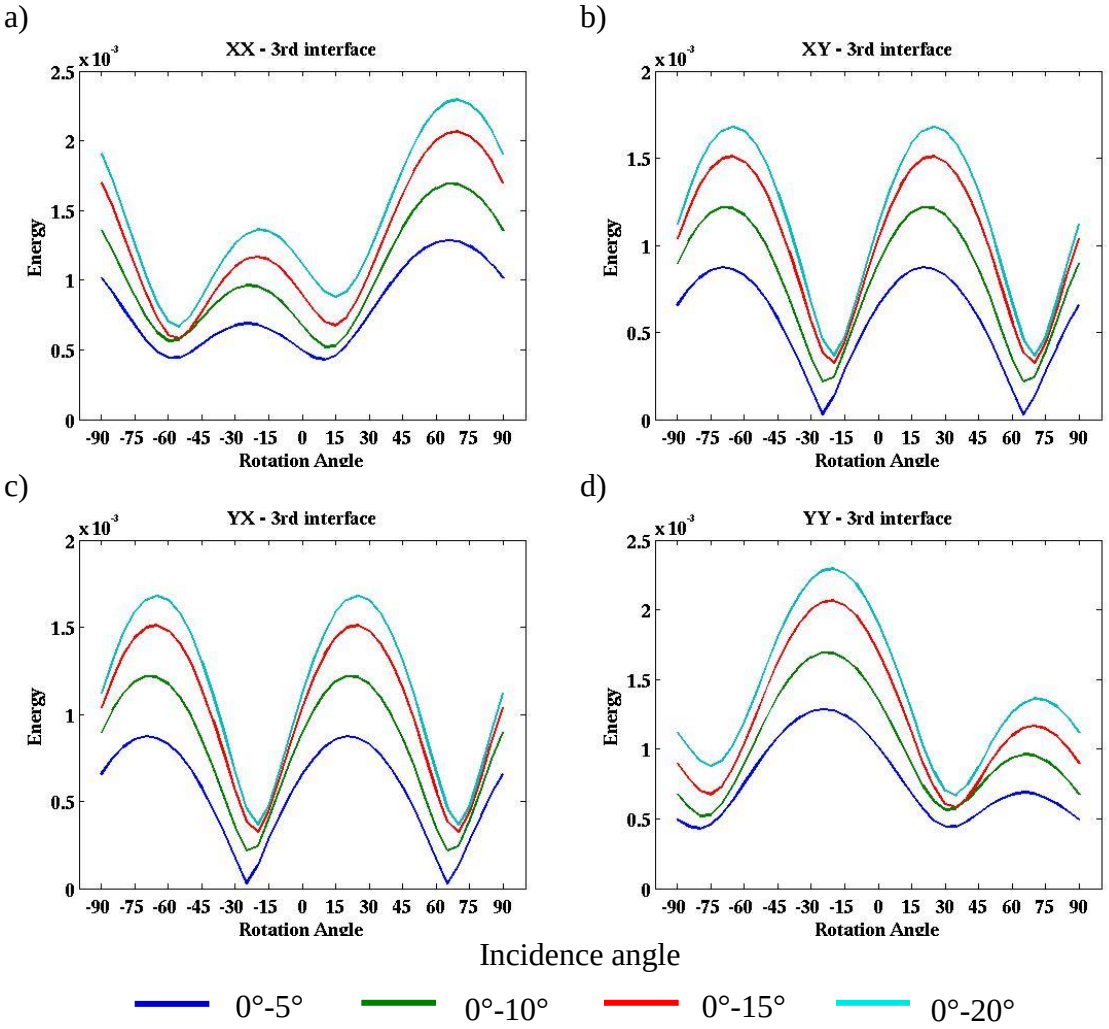

Figure 4.5: Energy calculated on (a) XX, (b) XY, (c) YX, and (d) YY components from interface C, an anisotropic-anisotropic interface, reflection for a range of rotation angles from -90° to 90° and an increasing range of incidence angles. For smaller ranges of incidence angles (0°-5°, blue line), off-diagonal component energy is minimized within 5° of the isotropy plane orientation in layer 3, 60°. Absolute maxima occur on diagonal components at orthogonal rotation angles, approximately 60° on the XX component and -30° on the YY component. A very strong imprint of the transmission through the anisotropic layer is observed.

Rotation analysis performed on the reflection from interface D is shown in Figure 4.6. Extrema are clear on off-diagonal components in Figure 4.6b and Figure 4.6c, but do not occur at the correct location and gradually vary by up to 30° as an increasing range of incidence angles are included in the energy calculations. Diagonal components in Figure 4.6a and Figure 4.6d do not show clear energy maxima, regardless of the range of incidence angles included in energy calculations. The orientation of the isotropy plane in layer 4 is at 0°, but the time lag accumulated in the overburden invalidates rotation analysis results for underlying anisotropy systems regardless of the range of incidence angles over which energy is calculated. Pre-existing time delays must be removed before shear wave polarizations can be analyzed in subsequent anisotropic layers.

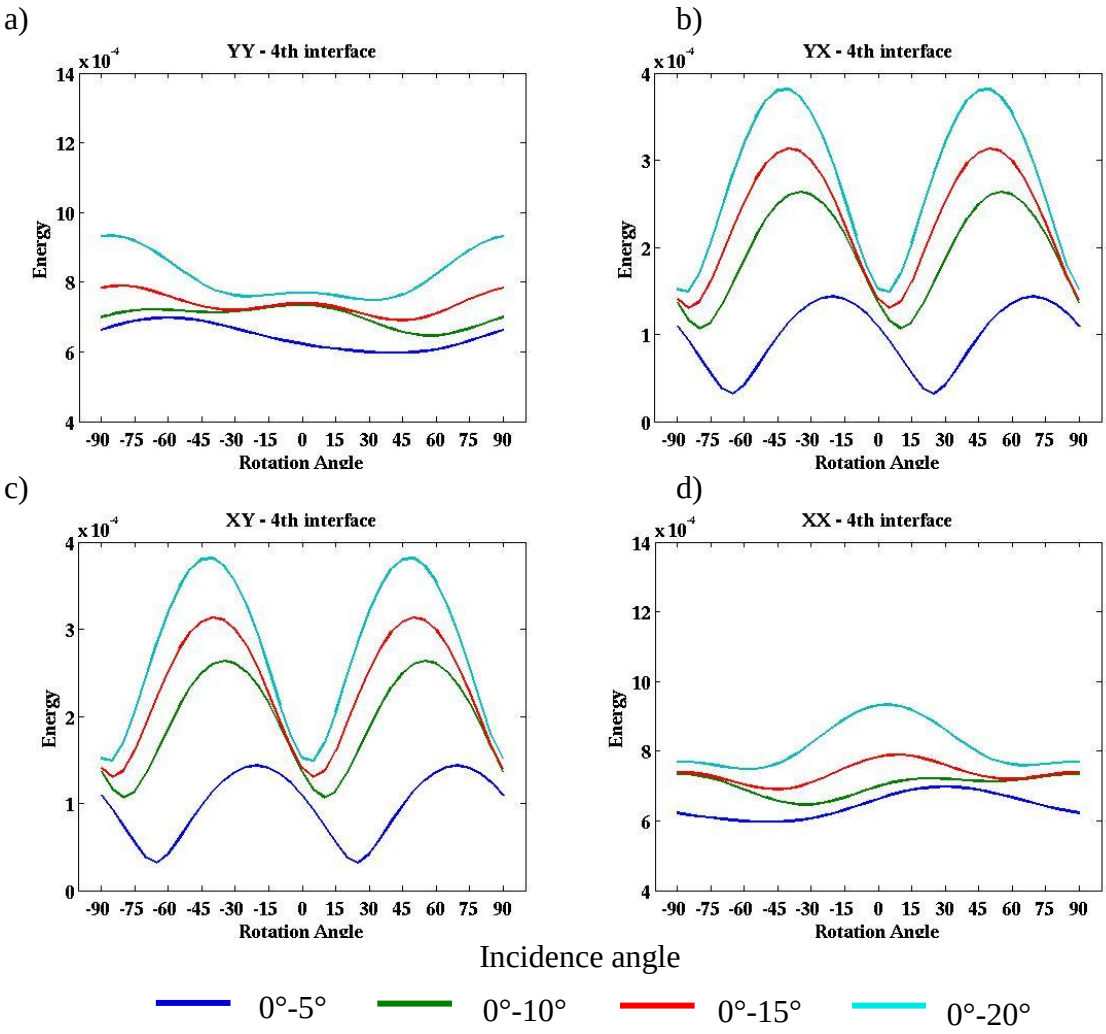

Figure 4.6: Energy calculated on (a) XX, (b) XY, (c) YX, and (d) YY components from interface D, an anisotropic-isotropic interface, reflection for a range of rotation angles from -90° to 90° and an increasing range of incidence angles. Energy minima are clear on off-diagonal components, but occur at the wrong locations. Clear energy maxima are not observed on diagonal components, which should correspond to the orientation of the isotropy plane in layer 4, 0°. The time lag accumulated in the overburden invalidates the rotation analysis results for underlying anisotropy systems regardless of the range of incidence angles over which energy is calculated.

Data are rotated 60° counterclockwise into alignment with the natural anisotropy system, as indicated by the rotation analysis performed on the near offsets of reflections at interfaces B and C (Figure 4.7). In these data, rotated into the coordinates of the natural anisotropy system, individual SV-SV and SH-SH reflectivity characteristics become apparent. The SV mode from the interface C reflection can be distinguished on the Y'Y' component in Figure 4.7d, arriving as the fast shear wave (S1) at approximately 4220 ms. A polarity reversal is observed near 1800 m (18° incidence angle) and corresponds to the zero crossing predicted by computed reflectivity curves. The SH mode from the same reflection is concentrated on the X'X' component in Figure 4.7a, arriving as the slow shear wave (S2) at approximately 4330 ms. The range of offsets in this survey is not large enough to observe the SH wave zero crossing. The total lag between the fast and slow shear modes is approximately 110 ms. A noticeable amount of energy remains on off-diagonal components for the third interface reflection even though the data has been rotated into the proper coordinate system. This residual off-diagonal energy is a result of the immediate underlying anisotropic layer. The situation is similar to the case of an isotropic-anisotropic reflection, where the underlying anisotropy system imparts a polarization upon incident reflected shear waves.

Because it is not possible to identify the correct angle at which diagonal component energy reaches a maximum and off-diagonal component energy reaches a minimum through rotation analysis performed on the interface D reflection (~5000 ms), it is also not possible to isolate each shear mode on individual components. Evidence of shear wave splitting is still visible in Figure 4.7 for the fourth interface reflection after the data has been rotated 60° counterclockwise, into the coordinates overlying anisotropy system. This event still appears split because the orientation of the anisotropy system in this layer differs from that in the overburden. Again, there is no angle at which each shear

wave arrives as a single, unsplit waveform on a single component. This requires a static time shift to remove all time delays associated with the shear wave splitting in overlying layers.

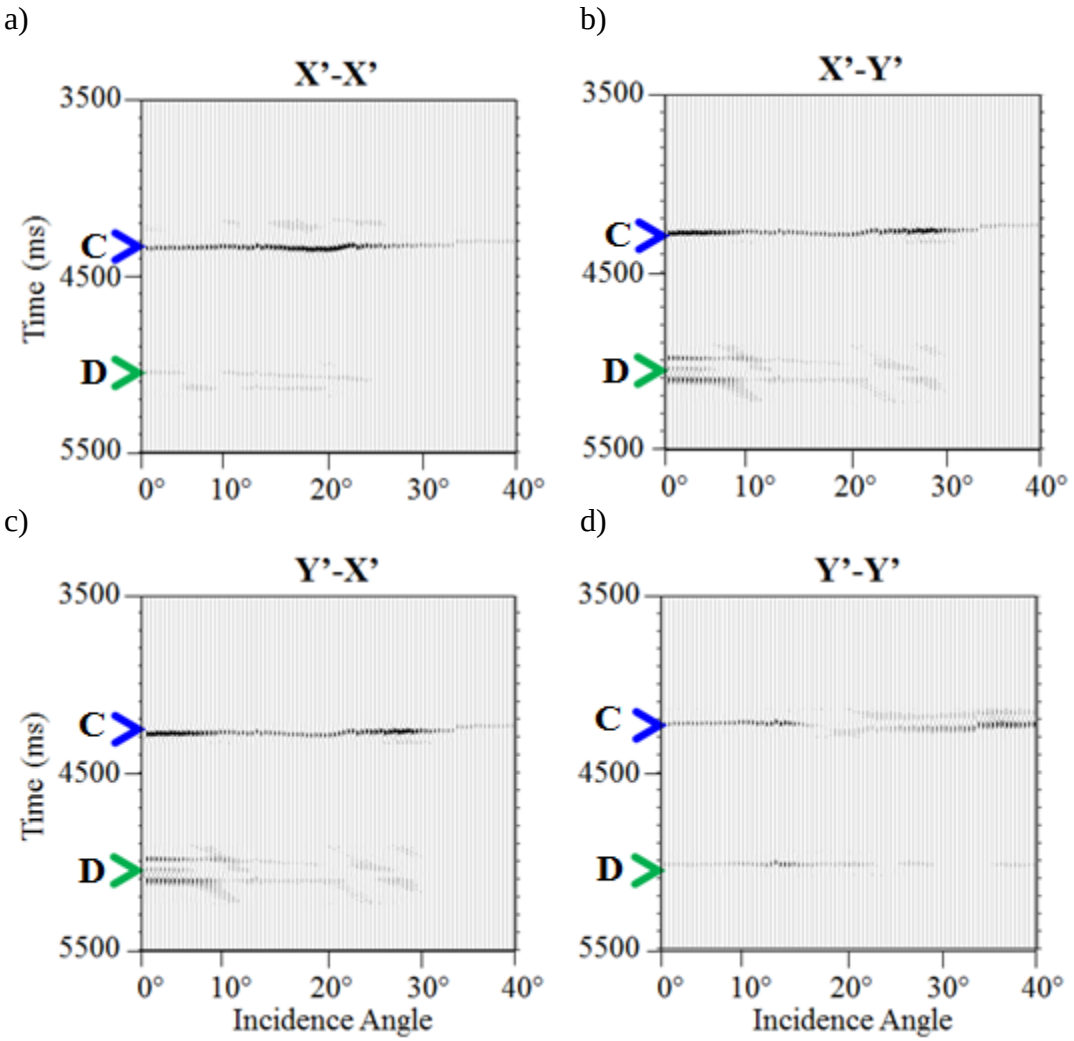

Figure 4.7: Shot gathers for (a) X'X', (b) X'Y', (c) Y'X', and (d) Y'Y' components along the x-axis (0°) after a 60° counterclockwise rotation applied over a time window from 3200 ms to the end of the record prior to polarization corrections. After rotation into layer three's natural anisotropy system coordinates, individual SV-SV and SH-SH reflectivity characteristics are apparent in the interface C reflection. The SV mode arrives on the Y'Y' component (d) as the fast shear wave (S1) at ~4220 ms. A polarity reversal near 1800 m (18° incidence angle) corresponds to the zero crossing predicted by computed reflectivity curves. The SH mode arrives on the X'X' component as the slow shear wave (S2) at ~4330 ms. The interface D reflection (green arrow), however, still exhibits effects of shear wave splitting because the orientation of anisotropy changes in the fourth layer.

4.3 LAYER STRIPPING AND ITERATIVE ROTATION ANALYSIS

A time lag of 116 ms was removed from the X'X' component, containing the slow shear wave, and a time lag of 60 ms was removed from both the X'Y' and Y'X' components. Removal of these time lags is the layer stripping process. After all time lags are removed, rotation analysis is repeated on the fourth interface. Figure 4.8 shows energy calculated from the post-layer stripping rotation analysis. Clear maxima now occur at angles of 30° and -60° on X'X' and Y'Y' components. Accordingly, X'Y' and Y'X' components now show minima at angles of 30° and -60°. The isotropy plane orientation in layer 4 is at 0°. As all data were previously rotated 60° (counterclockwise), a rotation through -60° (clockwise), therefore, corresponds to the orientation of the natural anisotropy system at 0° in the current coordinate system. Layer stripping has thus allowed for proper identification of the natural anisotropy system for this particular layer.

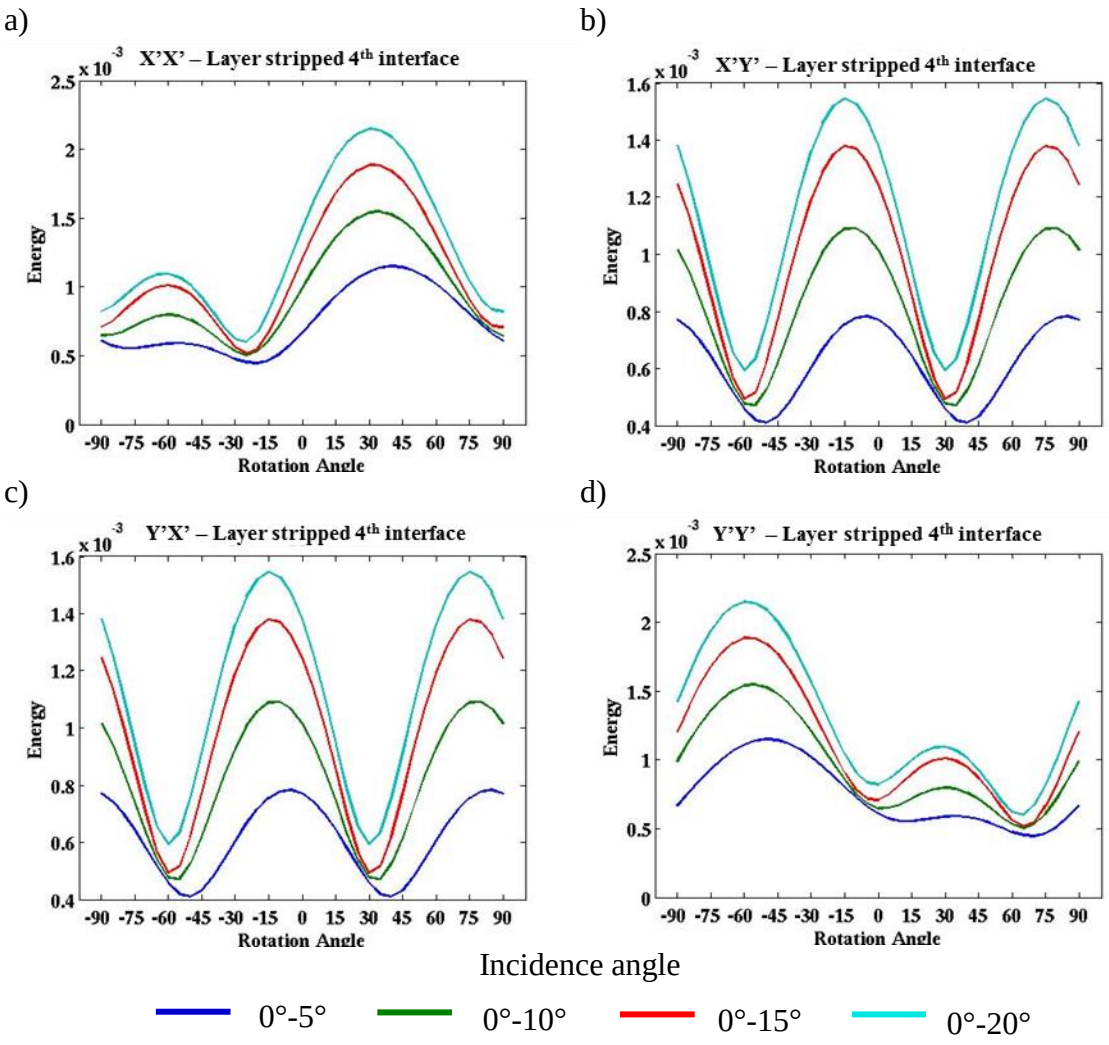

Figure 4.8: Energy calculated on (a) X'X', (b) X'Y', (c) Y'X', and (d) Y'Y' components from the interface D reflection for a range of rotation angles from -90° to 90° after layer stripping has removed time delays accumulated in the anisotropic overburden. Diagonal component energy maxima and off-diagonal component energy minima occur at an angle of -60° and 30°. The isotropy plane orientation in layer 4 is at 0°. A rotation through -60° therefore corresponds to the orientation of the natural anisotropy system in the current coordinate system.

When time lags are removed for all components for reflection C, all data below the third interface reflection are rotated 60° clockwise into the coordinates of the fourth layer's natural anisotropy system, results of which are shown in Figure 4.9. Eliminating effects of shear wave splitting from the third layer enables the use of iterative rotations to isolate individual fast and slow shear modes on diagonal components for subsequent reflections. In Figure 4.9, energy from the interface D reflection (green arrow) is contained primarily on the diagonal components after the rotation is performed. The fast shear wave (S1) arrives on the Y''Y'' (4.9d) component at approximately 4910 ms and consists primarily of SV energy. The slow shear wave (S2) arrives on the X''X'' (4.9a) component at approximately 5010 ms and consists primarily of SH energy. A major difference between the results of initial rotations performed on the interface C reflection and secondary rotations performed on the interface D reflection is that coherent energy from the fourth interface reflection is not visible on the off-diagonal components after rotation into the natural anisotropy system coordinates. Residual off-diagonal component energy was present after rotations performed on the third interface reflection. This residual energy resulted from the influence of the underlying anisotropy system. The fifth layer of the model is isotropic, so it does not impose an anisotropic overprint upon reflection at the fourth interface.

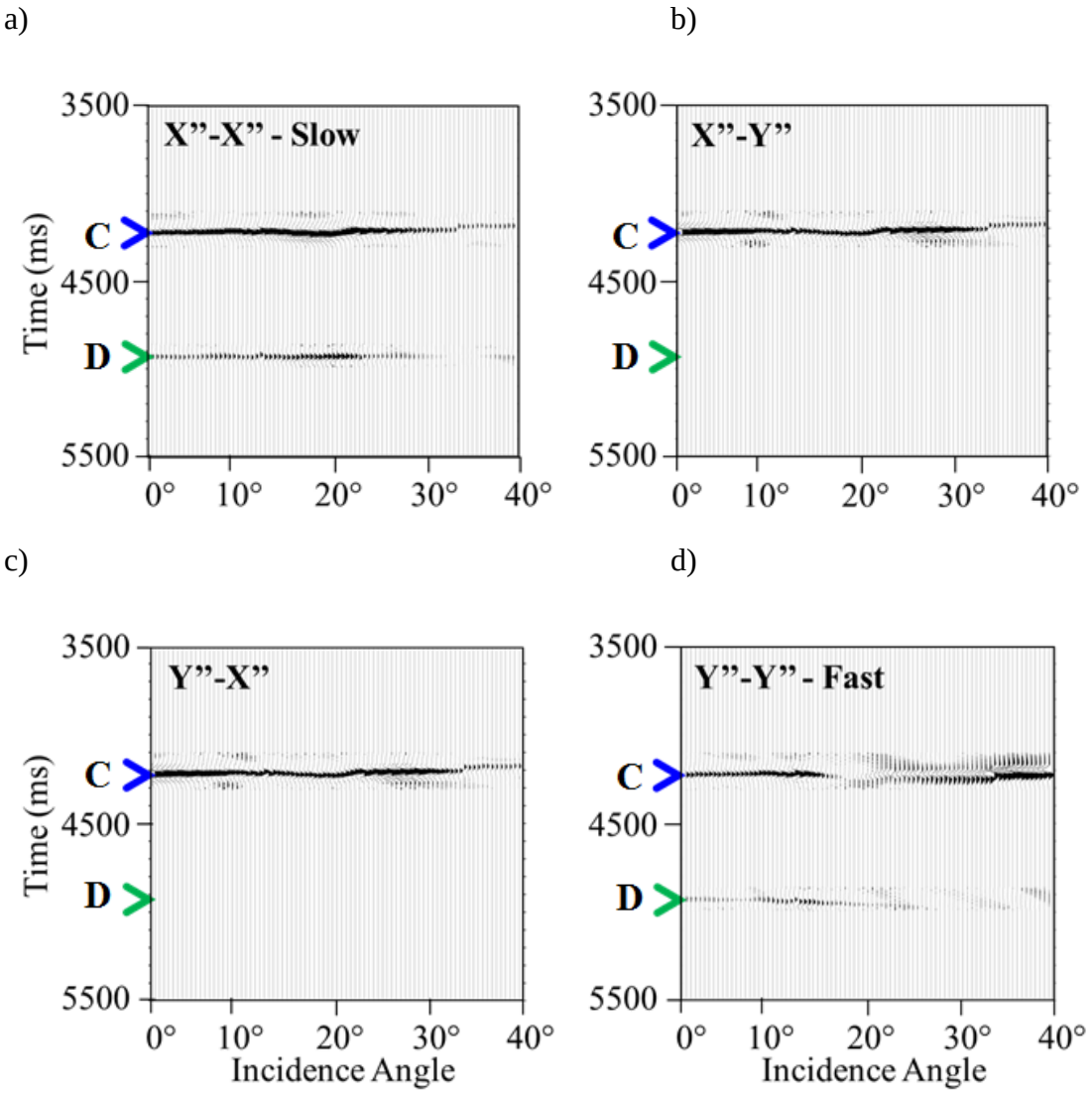

Figure 4.9: Shot gathers for (a) X’’X’’, (b) X’’Y’’, (c) Y’’X’’, and (d) Y’’Y’’ components along the x-axis (0°) after time delays are removed and a 60° clockwise rotation is applied to the interface D reflection (green arrow). Removing the effect of the anisotropic overburden allows reflections from subsequent layers to be separated into fast and slow shear modes on each diagonal component. The fast shear wave (S1) arrives on the Y’’Y’’ (a) component at ~4910 ms and consists primarily of SV energy. The slow shear wave (S2) arrives on the X’’X’’ (d) component at ~5010 ms and consists primarily of SH energy.

4.4 POLARIZATION CORRECTION

With SV and SH energy concentrated on separate diagonal components, the polarization correction is applied to its respective X''X'' or Y''Y'' component (Figure 4.10). The polarization correction effectively removes the SV-SV polarity reversal on the Y''Y'' component (Figure 4.10d). However, the correction cannot be applied within the immediate range of the zero-crossing (15°-20°), and amplitudes within that range remain weak to null. The zero-crossing for the SH-SH wave is outside the range of offsets included, and effects of the correction on this mode are less apparent. The $\tan^2\theta$ approximation used for the polarization correction becomes less accurate beyond 30° incidence angle, which may contribute to the amplitude variation that is observed even after the polarization correction is applied.

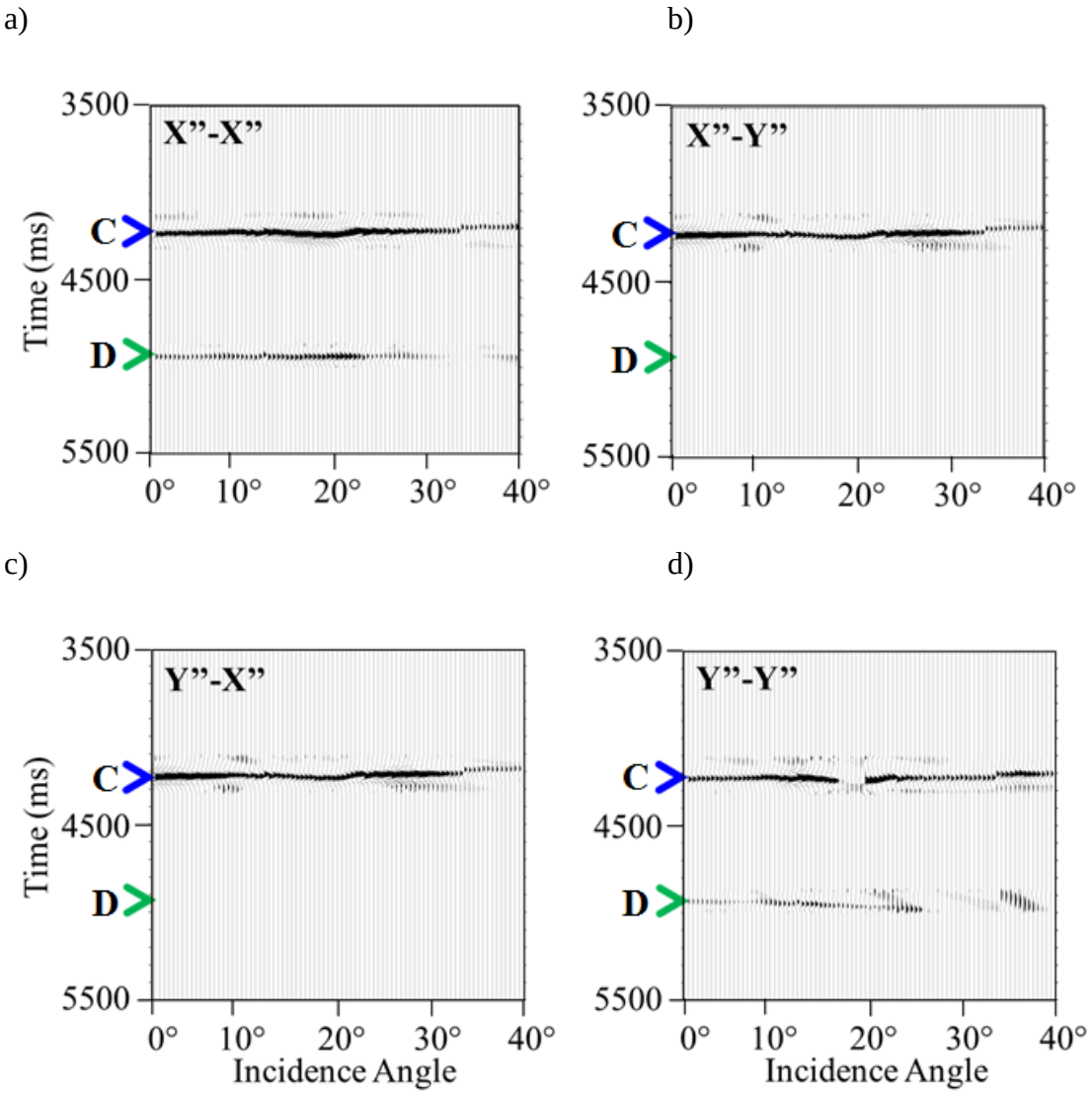

Figure 4.10: Shot gathers for (a) X’’X’’, (b) X’’Y’’, (c) Y’’X’’, and (d) Y’’Y’’ components after iterative rotations, time shifts, and amplitude corrections for polarization distortion. The SV-SV polarization correction, applied to the Y’’-Y’’ component removes the polarity reversal beyond ~20° incidence angle and normalizes all amplitudes to zero offset. Because the correction cannot be applied within the range of the zero-crossing (15°-20°), amplitudes within that range remain weak. The zero-crossing for the SH-SH wave is outside the range of offsets included, and effects of the correction on this mode are less apparent. Amplitudes across the full offset range, however, are normalized to zero offset, allowing proper rotation analysis.

To examine the effect the polarization correction has on traditional Alford (1986) rotation beyond normal incidence, polarization-corrected data are rotated back to original coordinates, and the rotation analysis is performed again in terms of energy extrema. The use of primes is no longer necessary because all results are presented relative to the original coordinate system and coincide with the true anisotropy orientation presented in the model described in Table 4.1. The results of the rotation analysis performed after the polarization correction, shown in Figures 4.11 and 4.12, differ in number of ways relative to results of rotation analysis performed prior to the polarization correction, shown in Figures 4.5 and 4.8.

Figure 4.11 shows the results of rotation analysis performed on the interface C reflection after amplitude corrections for polarization distortion have been applied. Energy calculations including incidence angles from 0-5° and 0-10° no longer exhibit two distinct maxima on each diagonal component and are no longer symmetric about the principal axes, as they did in results of rotation analysis performed prior to polarization corrections (Figure 4.5a and d). Maxima occur near 60° on the XX component and near -30° on the YY component. Energy calculations including incidence angles from 0-15° begin to show a small secondary local maximum at orthogonal rotation angles (-30° on XX and 60° on YY in Figure 4.11a and d), similar to that which was observed prior to polarization corrections (Figure 4.5a and d).

When incidence angles up to 20° are included in the energy calculations, a distinct maxima can be observed on the XX component at -30° and the YY component at 60°, and each diagonal component again exhibits symmetric behavior about the principal axes in Figure 4.11a and d. The location of the absolute maximum across individual XX and YY components differs from that which is observed prior to polarization corrections. Before the polarization correction, absolute maxima occurred near 60° on the XX

component and near -30° on the YY component (Figure 4.5a and d). After the polarization correction, absolute maxima occur at -30° on the XX component and at 60° on the YY component (Figure 4.11a and d). This difference is important to note when distinguishing between the isotropy plane and the symmetry axis. Absolute maxima on the YY component, occurring at 60°, correspond to the orientation of the isotropy plane and show a much larger increase in computed energy relative to energy calculations performed prior to the polarization correction. This is consistent with SV energy, which would be largely confined within the isotropy plane, occurring on the YY component after rotation into the natural anisotropy coordinates. A large increase in SV mode energy is expected because reflection strength of SV-SV waves decreases much faster with increasing incidence angles than for SH-SH waves. The polarization correction aims to normalize weaker reflections at wider incidence angles to values observed at normal incidence. Therefore, the location of the absolute maximum in rotation analysis performed on polarization-corrected reflections corresponds to the location of the isotropy plane, containing SV energy and the location of the secondary maximum corresponds to the location of the symmetry plane, containing SH energy. An additional benefit is that for energy calculations including incidence angles up to 20°, the location of the absolute maxima on each diagonal component is also closer to the true orientation of the principal axes after the polarization correction is implemented in the rotation analysis.

Off-diagonal component energy calculations from rotation analysis performed after the polarization correction is applied (Figure 4.11b and c) show considerably less variation from those performed prior to the polarization correction (Figure 4.5b and c) because the correction operates primarily on SV-SV and SH-SH energy. The location of off-diagonal minima and computed energy values are consistent prior to and after the polarization correction is applied for calculations including incidence angles up to 15°.

For calculations including incidence angles up to 20°, diagonal component energy maxima and off-diagonal component energy minima occur closer to the true orientation of the principal axes after the polarization correction is applied.

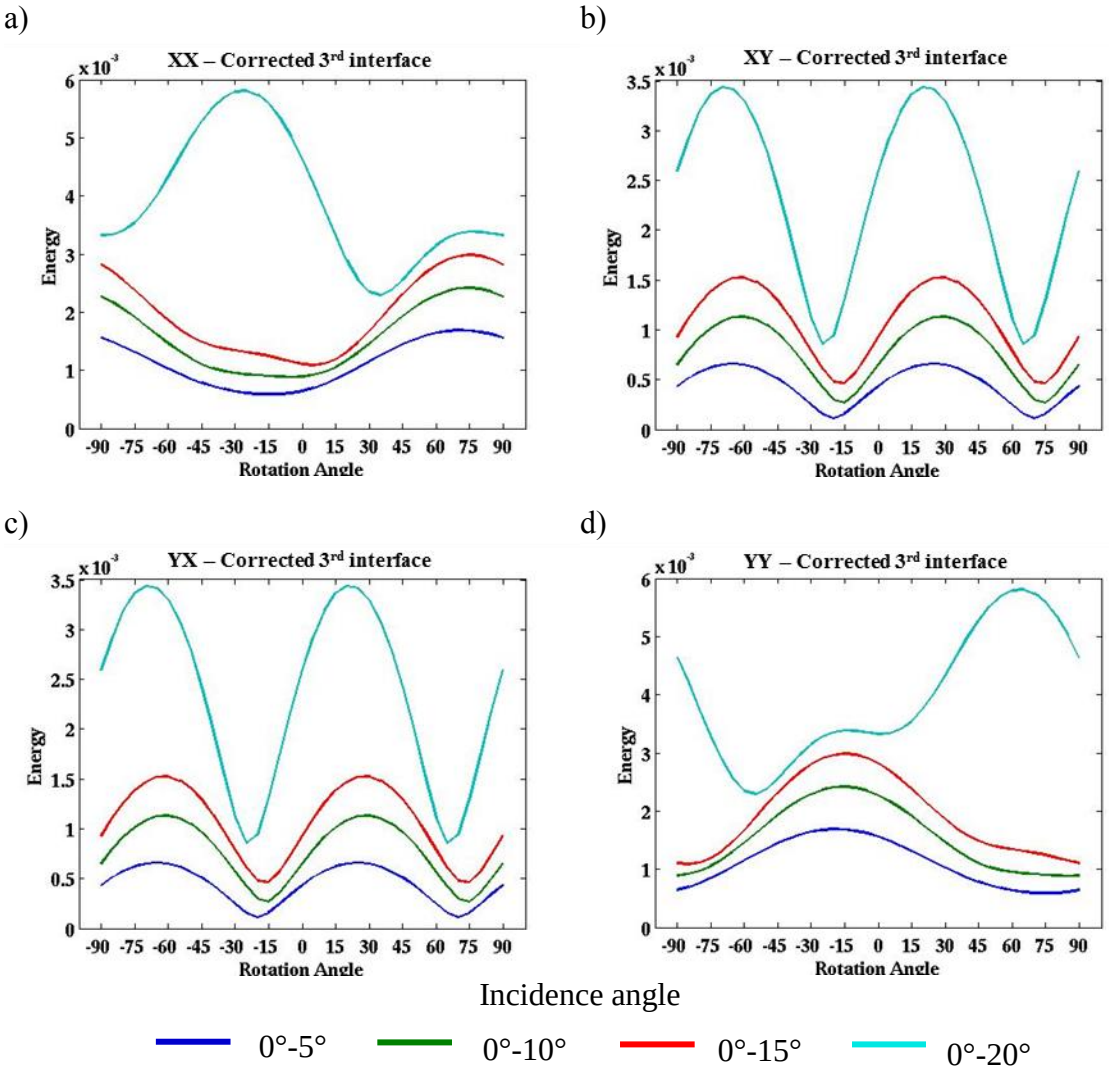

Figure 4.11: Alford rotation analysis performed on the interface C reflection after amplitude corrections for polarization distortion have been applied. For energy calculations including incidence angles up to 20°, the location of the diagonal component energy maxima and off-diagonal component energy minima are closer to the true orientation of the principal axes compared to results of Alford (1986) rotation analysis performed on data that has not been corrected for polarization distortion (Figure 4.5). The polarization correction also allows individual SV and SH mode energy associated with the respective isotropy plane and symmetry axis to be more clearly distinguished.

Figure 4.12 shows the results of rotation analysis performed on the interface D reflection after layer stripping has removed all time delays and amplitude corrections have been applied for polarization distortion. Diagonal component energy maxima and off-diagonal component energy minima now occur at 0° and 90°, coincident with the orientation of the natural anisotropy system in layer 4. The polarization correction has produced similar results to that which was observed in Figure 4.11. After applying the polarization correction, energy calculations including incidence angles up to 20° distinguish individual SV and SH mode energy associated with the respective isotropy plane and symmetry axis. Furthermore, relative to rotation analysis performed before polarization corrections (Figure 4.8), energy calculations including incidence angles up to 20° better localize diagonal component energy maxima and off-diagonal component energy minima closer to the true orientation of the principal axes after the polarization correction is applied.

Overall, rotation analysis performed on data that has been corrected for polarization distortion results in larger calculated values of energy. As a wider range of incidence angles are included in the energy calculations, the total energy computed from the polarization-corrected data increases relative to energy computed from uncorrected data. This result is consistent with the modus operandi. The correction aims to normalize amplitudes, which decrease with increasing incidence angle, to normal-incidence values. Thus, it is as expected that the total energy in each component increases after the polarization correction is applied.

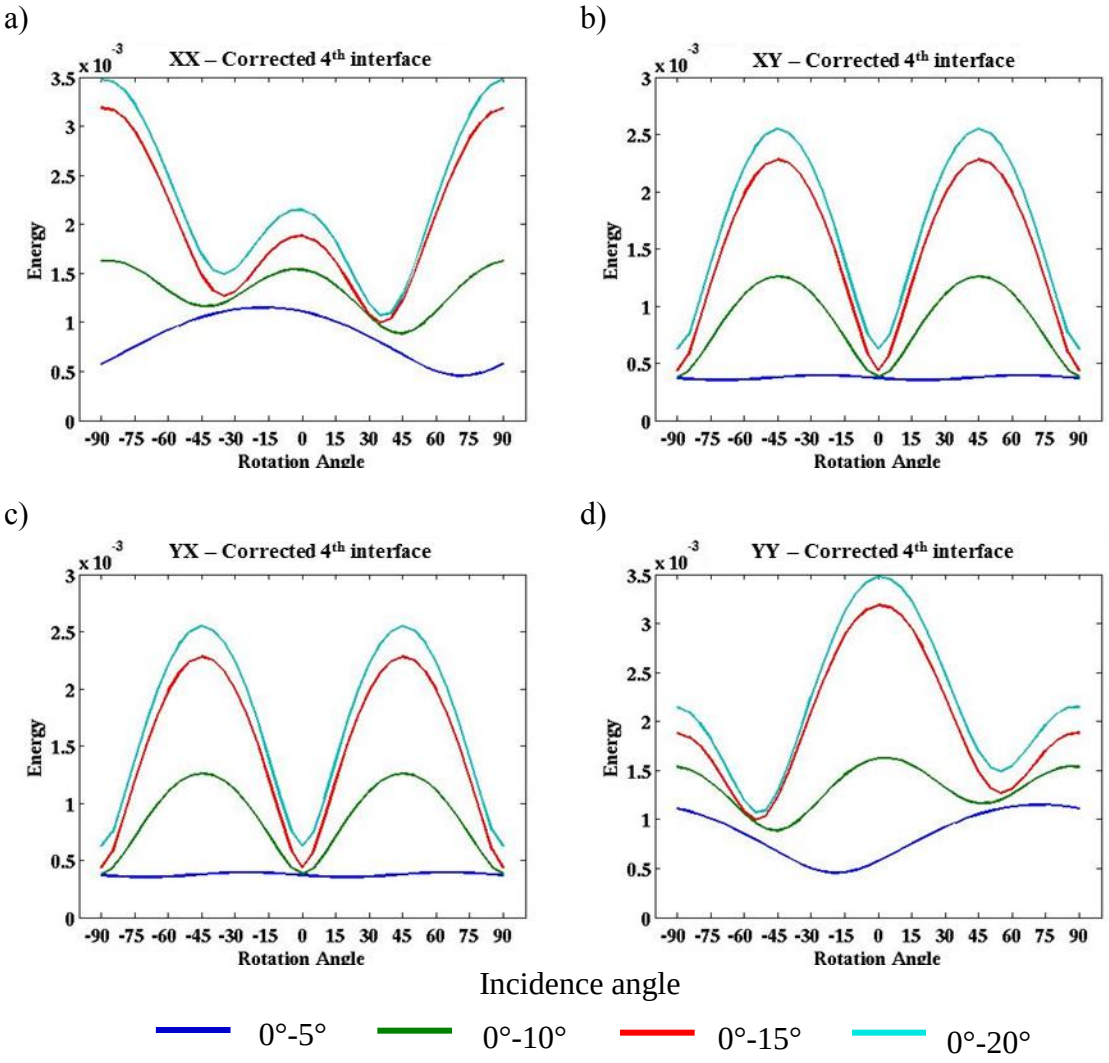

Figure 4.12: Alford rotation analysis performed on the interface D reflection after layer stripping has removed all time delays accumulated in the anisotropic overburden and the polarization correction has normalized all amplitudes to normal-incidence values. Energy calculations including incidence angles up to 20° localize diagonal component energy maxima and off-diagonal component minima closer to the true orientation of the principal axes relative to results of Alford (1986) rotation analysis performed on data that has not been corrected for polarization distortion (Figure 4.8). The polarization correction also helps to better distinguish individual SV and SH mode energy associated with the respective isotropy plane and symmetry axis.

Chapter 5: Conclusions

For the simplicity of this study, horizontal transverse isotropy (HTI) caused by vertical, aligned cracks, fractures, and subsurface stresses is considered without regard to the presence of vertical transverse isotropy (VTI), a property likely inherent to most layered media. To be complete, the combination of HTI and VTI would result in orthorhombic symmetry. The mathematical complexities introduced by this order of symmetry are beyond the scope of this study and the present state of technology, but they would certainly affect the seismic response and may alter the effectiveness of the polarization correction. The layered nature of HTI media used in this study certainly affects the relative success with which off-diagonal component energy is minimized for isotropic-anisotropic, anisotropic-anisotropic, and anisotropic-isotropic interfaces during rotation analysis. This effect is apparent in results from the rotation scan analysis and the rotations subsequently applied to the seismic data, whereby the underlying anisotropy system imparts a degree of its anisotropic character upon the incident reflected wave without the wave actually travelling through the underlying anisotropic medium. Polarization upon reflection mitigates efforts to eliminate off-diagonal component energy for reflections from isotropic-anisotropic and anisotropic-anisotropic interfaces. One way to address lower orders of symmetry would be to perform a full 9-component tensor rotation. This would require use of not only the S-wave data, but the P-wave data as well.

Additionally, a single layer with conjugate fractures would also result in orthorhombic symmetry. Proper characterization of conjugate fracture sets, which are an equally common occurrence, would significantly improve hydrocarbon recovery, particularly if only one set of the conjugate fractures is open to fluid flow, while the other is cemented.

The success of the polarization correction largely depends on the accuracy of shear wave reflectivity approximations. The SV reflectivity approximation, which makes use of a $\sin^2$ term, provides a very close fit to the true Zoeppritz equations. The correction thus successfully removes the SV polarity reversal, but cannot be applied in the immediate range of the zero-crossing. Conversely, the SH reflectivity approximation, which makes use of a $\tan^2\theta$ term, begins to diverge from the true Zoeppritz equations near 30° incidence angle. The location of the zero-crossing differs by as much as 10° between the true Zoeppritz equations and the $\tan^2\theta$ approximation. The disagreement between Zoeppritz reflectivity curves and the $\tan^2\theta$ approximation certainly reduces the effectiveness of the SH polarization correction. Use of a higher order approximation by including an additional trigonometric term to better fit true SH reflectivity behavior might yield better results.

In a less idealized setting, this process would be limited by both data quality and geologic conditions. Significant noise may lead to ambiguous results during rotation analysis. Furthermore, if changes in anisotropy orientation do not coincide with the impedance contrasts that give rise to continuous reflections, layer-stripping may produce misleading results. For example, the time delay accumulated in a thin, highly anisotropic layer of weak to no reflectivity would be averaged over the interval between the nearest reflections, leading to an incorrect interpretation of thick layers with minimal anisotropy.

Nonetheless, for the model presented here, iterative rotations, combined with subtraction of all slow shear wave time lags, concentrated SV and SH energy on individual diagonal components and removed the effects of anisotropic overburden. The polarization correction equalized amplitudes across all offsets and eliminates the SV polarity reversal, which can have destructive consequences in the stacking process. After the polarization correction is applied, increasing the range of incidence angles used in

energy calculations to 20° more effectively distinguishes individual SV and SH mode energy, allowing for allowing for more distinct identification of the isotropy plane and the symmetry axis. Increasing the range of incidence angles used in energy calculations to 20° also localizes diagonal component energy maxima and off-diagonal component energy minima closer to the true orientation of the principal axes after the polarization correction is applied. This allows for more effective characterization of fracture strike, intensity, and lateral variability with shear wave attributes derived from 3D-9C seismic data such as polarization, delay time, and normal incidence reflection coefficient.

References

Aguilera, R., 1980, Naturally Fractured Reservoirs: PennWell Publishing Company.

Alford, R. M., 1986, Shear data in the presence of azimuthal anisotropy, Dilley, Texas: 56th Annual Meeting, SSEG, Expanded Abstracts, 476-479.

Aki, K. and P. G. Richards, 2002, Quantitative seismology, 2nd ed.: University Science Books

Beckham, W. E., 1996, Seismic anisotropy and natural fractures from VSP and borehole sonic tools – A field study: Geophysics, 61, 456-466.

Booth, D. C., and S. Crampin, 1985, Shear-wave polarization on a curved wave front at an isotropic free surface: Geophysical Journal of the Royal Astronomical Society, 83, 31-45.

Campbell, T. and R. H. Tatham, 2011, Correction for distortion in polarization of reflected shear-waves in isotropic and anisotropic media, Expanded Abstracts, 81st Annual Intl. Mtg, Soc. of Explor. Geophysicists, 30, 1333-1337.

Campbell, T. and R.H. Tatham, 2012 Corrections for polarization distortion in reflected shear waves and possible extensions to the Alford rotation at non-normal incidence angles and applications-, Expanded Abstracts, 82nd Annual Intl. Mtg. Soc. of Explor. Geophysicists, 31, MS E-P1-1.8.

Campbell, T., and R. H. Tatham, 2013, Rotation of Shear-Wave Components at Non-Normal Angles of Incidence: 75th EAGE Conference & Exhibition, Extended Abstracts, TU0201.

Cliet, C., L. Brodov, A. Tikhonov, D. Marin, and D. Michon, 1991, Anisotropy survey for reservoir definition: Geophys. J. Int., 107, 417-427.

Crampin, S., 1985, Evaluation of anisotropy by shear-wave splitting: Geophysics, 50, 142-152.

Davis, T. L., and C. Lewis, 1990, Reservoir characterization by 3-D, 3-C seismic imaging, Silo Field, Wyoming: The Leading Edge, 9, 22-25.

Garotta, R., and P. Y. Granger, 1988, Acquisition and processing of 3Cx3-D data using converted waves: 58th Annual Meeting, SEG, Expanded Abstracts, S13.2.

Gumble, J. E. and J. E. Gaiser, 2006, Characterization of layered anisotropic media from prestack PS-wave-reflection data: Geophysics, 71, D171-D182.

Haacke, R. R., G. K. Westbrook, and S. Peacock, 2009, Layer-stripping of shear-wave splitting in marine PS waves: Geophys. J. Int., 176, 782-804.

Harrison, M. P., and R. R. Stewart, 1993, Poststack migration of P-SV seismic data: Geophysics, 58, 1127-1135.

Hickman, S. H., M. D. Zoback, and J. H. Healy, 1988, Continuation of a deep borehole stress measurement profile near the San Andreas fault: 1. Hydraulic fracturing stress measurements at Hi Vista, Mojave Desert, California: Journal of Geophysical Research, 93, 15183-15195.

Lefeuvre, F., L. Nicoletis, V. Ansel, and C. Cliet, 1992, Detection and measure of the shear-wave birefringence from vertical seismic data: theory and applications: Geophysics, 57, 1463-1482.

Lefeuvre, F. and J. H. Queen, 1992, Propagator matrix processing single source 3-component VSPs: 62 Annual Meeting, SEG, Expanded Abstracts, 163-168.

Lefeuvre, F., R. Turpening, C. Caravana, A. Born, and I. Nicoletis, 1993, Vertical open fractures and shear-wave velocities derived from VSPs, full waveform acoustic logs, and televiewer data: Geophysics, 58, 818-834.

Li, X., 1997, Fractured reservoir delineation using multicomponent seismic data: Geophysical Prospecting, 45, 39-64.

Li, X., and S. Crampin, 1993, Linear-transform techniques for processing shear-wave anisotropy in four-component seismic data: Geophysics, 58, 240-256.

Liu, E. and S. Crampin, 1990, Effects of the internal shear wave window: Comparison with anisotropy induced splitting: Journal of Geophysical Research, 95, 11275-11281.

Liu, E., S. Crampin, and G. Yardley, 1990, Polarizations of reflected shear-waves: Geophysical Research Letters, 17, 1137-1140.

Lynn, H. B., and L. Thomsen, 1986, Shear-wave exploration along the principal axes: 56th Annual Meeting, SEG, Expanded Abstracts, 473-476.

Lynn, H. B., and L. Thomsen, 1990, Reflection shear data collected near the principal axes of azimuthal anisotropy: Geophysics, 57, 1463-1481.

Lyons, E. S., 2006, Polarization rotation upon reflection of direct shear waves in purely isotropic media, MS Thesis, University of Texas at Austin.

MacBeth, C. and S. Crampin, 1991, Examination of a spectral method for measuring the effects of anisotropy: Geophysical Prospecting, 39, 667-689.

Mallick, S., and L. N. Frazer, 1987, Practical aspects of reflectivity modeling: Geophysics, 52, 1355-1364.

Mattocks, B. W., 1998, Borehole geophysical investigation of seismic anisotropy at Vacuum Field, Lea County, New Mexico, MS Thesis, Colorado School of Mines.

Mueller, M., 1991, Prediction of lateral variability in fracture intensity using multicomponent shear-wave surface seismic as a precursor to horizontally drilling in Austin chalk: Geophys. J. Int., 107, 409-415.

Nelson, R. A., 1985, Geologic Analysis of Naturally Fractured Reservoirs: Gulf Publishing Company, Houston.

Queen, J. H., F. Lefeuvre, J. B. Sinton, V. D. Cox, and P. L. Buller, 1992, Vertical delineation of natural fracture orientation and density using 9-component VSP data from Conoco test facility: 5th International Workshop on Seismic Anisotropy, Abstract 15.

Spratt, R. S., N. R. Goins, and T. J. Fitch, 1993, Psuedo-shear – The analysis of AvO, in Backus, M. M., ed. Offset-dependent reflectivity – theory and practice of AVO analysis, 37-56. Soc. of Expl. Geophys.

Ruger, A., 2002, Reflection coefficients and azimuthal AVO analysis in anisotropic media. SEG geophysical monograph series, number 10, Society of Exploration Geophysicists, 190 p.

Tatham, R .H. and M. D. McCormack, 1991, Multicomponent seismology in petroleum exploration: SEG, ed. E. B. Neitzel and D. F. Winterstein.

Thomsen, L. A., 1986, Weak elastic anisotropy: Geophysics, 51, 1954-1966.

Thomsen, L. A., 1988, Reflection seismology over azimuthally anisotropic media: Geophysics, 53, 304-314.

Thomsen, L., Tsvankin, I., and Mueller, M., 1999, Coarse-layer stripping of vertically variable azimuthal anisotropy from shear wave data: Geophysics, 64, 1126-1138.

Warpinski, N. R. and L. W. Teufel, 1991, In situ stress measurements at Rainer Mesa, Nevada Test Site – influence of topography and lithology on the stress state in tuff: International Journal of Rock Mechanics & Mining Science and Geomechanical Abstracts, 28, 143-161.

White, J. E., 1983, Underground sound: Application of sound waves: Elsevier Science Publishing Co.

Winterstein, D. F., and M. A. Meadows, 1991a, Shear-wave polarizations and subsurface stress directions at Lost Hills field: Geophysics, 56, 1331-1348.

Winterstein, D. F., and M. A. Meadows, 1991b, Changes in shear-wave polarization azimuth with depth in Cymric and Railroad Gap oil fields: Geophysics, 56, 1349-1364.

Yardley, G. S. and S. Crampin, 1991, Extensive-dilatancy anisotropy: relative information in VSPs and reflection surveys: Geophysical Prospecting, 39,337-355.

Yardley, G. S., G. Graham, and S. Crampin, 1991, Viability of shear-wave amplitude versus offset studies in anisotropic media: Geophysical Journal International, 107, 493-503.

Zoeppritz, K., 1919, Erdbebenwellen VIIIB, On reflection and propagation of seismic waves: Gottinger Nachrichten, I, p. 66-84.

Vita

Jacqueline Patrice Maleski was born in Chicago, Illinois and later moved to Woodstock, Georgia. She graduated from Sequoyah High School in 2008. She then attended the University of Georgia, graduating with a Bachelor of Science in Geology in 2012. In 2014, she graduated from the University of Texas at Austin with a Master of Science in Geological Sciences.

Permanent e-mail address: maleskijp@gmail.com

This thesis was typed by Jacqueline Maleski.